CHAPTER 6

Modeling the Steady-State and Dynamic Characteristics of Solid-Oxide Fuel Cells

Robert J. Kee,* **Huayang Zhu, Robert J. Braun,** and **Tyrone L. Vincent**

Contents

Engineering Division, Colorado School of Mines, Golden, Colorado, USA
* Corresponding author, E-mail address: rjkee@mines.edu

Advances in Chemical Engineering, Volume 41
ISSN 0065-2377, DOI: 10.1016/B978-0-12-386874-9.00010-5

Abstract This chapter begins by introducing solid-oxide fuel-cell systems, including a description of balance-of-plant components and alternative cell architectures. Following a discussion of basic fuel-cell functions, a modeling framework is described in the context of a physically based mathematical representation of transport, chemistry, and electrochemistry. Recognizing the importance of dynamic behavior, the relevant conservation equations are presented in transient form. Using tubular and planar cells as examples, model problems are solved to illustrate and discuss both dynamical and steady-state behaviors. The models can be exercised in alternative ways to support different objectives. For example, model-based electrochemical impedance spectroscopy can assist interpreting dynamical behaviors in physical and chemical terms, providing a powerful alternative to equivalent-circuit modeling. Another important objective is to develop models that support model-predictive control strategies, coordinating multiple sensors and actuators, and respecting multiple constraints on actuation or responses.

1. INTRODUCTION

Compared to combustion or other fuel-cell technologies, solid-oxide fuel cells (SOFC) offer numerous potential benefits in converting fuels to electricity. The advantages include relatively high efficiency, high-grade waste heat, and low emissions. Because the potential advantages are so

attractive, SOFC technology is being developed at scales ranging from 50 W to 500 MW. The technology is envisioned for applications ranging from portable and mobile power systems that include truck auxiliary power units and unmanned vehicles, to combined heat and power for buildings and eventually in utility-scale central power plants. However, numerous challenges remain to be overcome before commercially viable technology is readily available.

Compared to polymer-electrolyte membrane (PEM) fuel cells, SOFCs operate at much higher temperatures (around 800°C). The high temperature leads to advantages and disadvantages. SOFCs are fuel flexible, enabling the use of synthesis gas (H_2 and CO) as well as some hydrocarbons. Because of the high temperature, precious-metal catalysts are not required. However, high-temperature degradation processes cause performance loss and limit lifetime. Depending on cell architecture, the thermal inertia of metal and ceramic components can lengthen start-up and shutdown procedures as well as limit the SOFC capability to follow rapid demand transients.

Although much attention is devoted to the fuel cell itself, the SOFC is only one component of a relatively complex system. The so-called balance of plant (BOP) includes fuel pumps, air blowers, hydrocarbon fuel reformers, tail-gas combustors, and heat exchangers. In fact, the chemistry and transport within components such as the reformer can be as complex as those within the SOFC. If electricity is the only product, then an SOFC system can produce efficiencies in excess of 50%. However, in certain settings, overall efficiency can be improved by taking advantage of the high temperature. For example, combined heat and power systems (CHP) can produce steam or hot water in addition to electricity. Of course, the BOP for a CHP system is different from that for a system that produces only electricity.

Figure 1 illustrates one of many possible process-flow diagrams for an SOFC system. The illustrated system shows fresh hydrocarbon fuel being compressed, desulfurized, and mixed with anode exhaust gases (typically H_2O, CO_2, H_2, and CO) before entering a catalytic fuel reformer. The endothermic reforming chemistry is supported by the catalytic combustion of a mixture of exhaust gases from the SOFC anode and exhaust oxygen-depleted air from the cathode. As illustrated, the reactor is configured to closely integrate the functions of a steam reformer and heat exchanger. The reformed fuel (dominantly H_2 and CO) enters the anode side of the SOFC. Fresh air, which is often supplied in excess of the stoichiometric requirements needed to support the electrochemical reactions, can be used to maintain the operating temperature. The air enters the cathode side of the SOFC through a recuperating heat exchanger that is configured to preheat incoming air with hot exhaust from the integrated reformer. Achieving high overall system efficiency depends upon close integration of the fuel-cell stack and BOP components. As the

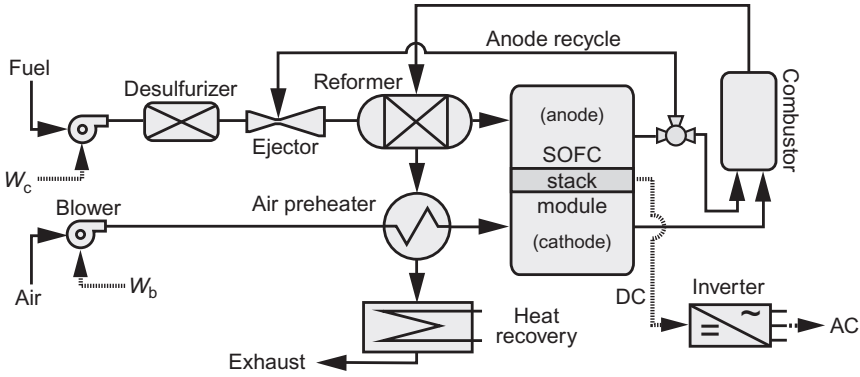

Figure 1 SOFC system process-flow diagram, showing integrated reactors and heat exchangers.

power demands on the fuel cell vary, it is usually important to control operating voltage and gas-flow rates so as to maintain the highest possible efficiency.

The fuel cell itself has at least three underlying characteristic timescales. The longest timescale (order of many minutes) is the result of thermal capacity in the ceramic and metal components. The heating and cooling rates affect the temperature, and hence the chemistry. The next timescale (order of a second) is the result of gas-flow residence time within the cell. As the cell operating conditions change, fuel and oxygen are consumed at different rates. The rates at which the gas-phase compositions change depend upon flow conditions. The shortest timescale (nearly instantaneous) is associated with the electrochemistry. That is, the cell voltage responds very rapidly to changes in electric current produced. Control strategies should be at least cognizant of these timescales and their interrelationships. Model-predictive control (MPC) seeks to incorporate predictive knowledge of the relevant physical and chemical phenomena directly into optimal control strategies.

Modeling and simulation play important beneficial roles in accelerating SOFC technology development. There is a vast and growing literature concerning most aspects of SOFC science and technology. However, the literature is concerned primarily with steady-state performance. The present writing incorporates both stationary and transient models.

1.1 SOFC architectures

Although the operating principles are similar, several different fuel-cell architectures are being developed. Figure 2 illustrates the salient attributes of a counterflow planar SOFC stack. This particular configuration is

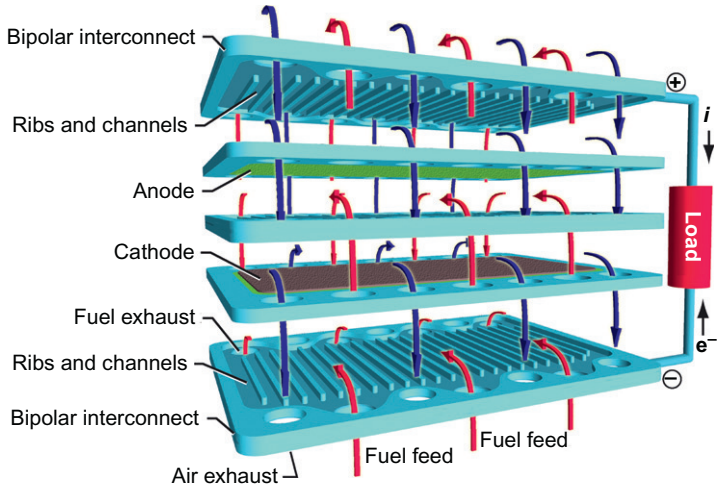

Figure 2 Exploded section of a planar SOFC stack.

modeled after a system developed in Germany at Forschungszentrum Jülich (Gubner *et al.*, 2006). The membrane-electrode assembly (MEA) typically is comprised of a porous composite Ni–YSZ anode support (order 1 mm thick), a dense YSZ electrolyte membrane (order 10 μm), and a composite LSM–YSZ cathode (order 20 μm). Fuel and air are introduced through a manifold of circular passages that carry gases from below. Exhaust is collected on the opposite side of the feed and directed downward via similar circular passages. The metal ribs that form the flow channels also contact the electrodes forming the electrical interconnect between MEA layers. Fuel flows on the anode side of the MEA and oxidizer flows on the cathode side. Under typical conditions, each cell layer operates at about 0.7 V. A typical stack may consist of some 50 layers connected electrically in series, producing a stack voltage of around 35 V. Among all the alternatives, planar architectures usually deliver the highest volumetric power density.

Figure 3 illustrates a tubular stack. The tubes are typically fabricated as a Ni–YSZ support, with a thin YSZ membrane and LSM–YSZ composite cathode applied onto the outside of the tube. Fuel flows within the tubes and air circulates over the outsides of the tubes. Cathode current collection is usually established easily by wrapping wires around the outsides of the tubes. However, anode current collection inside the tubes can be a significant technical challenge. As in the planar case, each tube usually operates at around 0.7 V. Assuming that the tubes are connected electrically in series, the 72-tube stack illustrated in Figure 3 would operate at around 50 V.

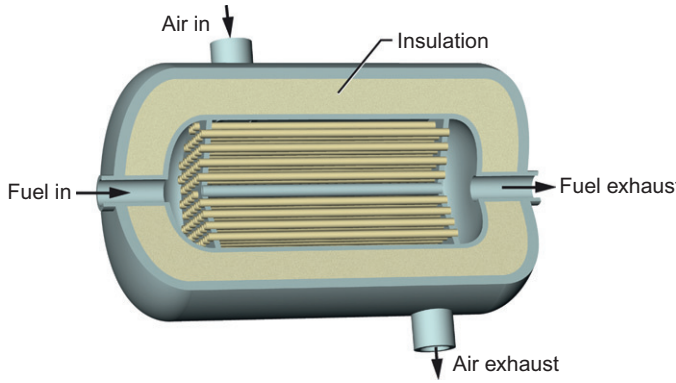

Figure 3 Illustration of a tubular SOFC stack.

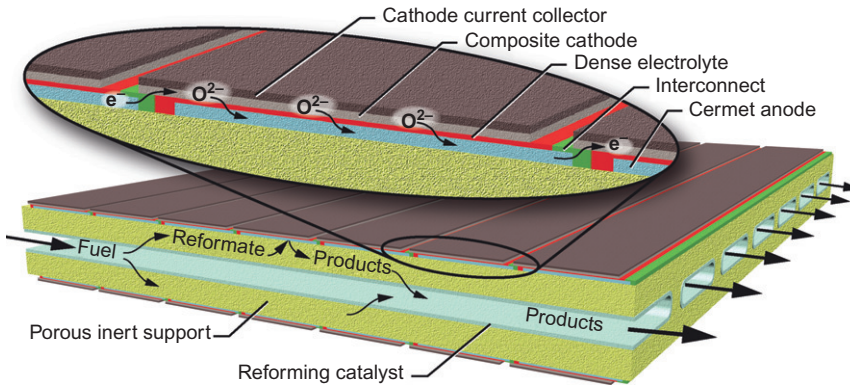

Figure 4 Section of an SIS-SOFC stack.

Tubular stacks can be configured with large or small tubes. Small-tube stacks producing power on the order of a kilowatt have low thermal inertia, and hence rapid start-up and shutdown transients as well as rapid response times (Howe *et al.*, 2011). As with planar stacks, tubular systems are being developed commercially by a number of companies.

Figure 4 illustrates the salient features of a planar segmented-in-series (SIS) module (Pillai *et al.*, 2007; Zhu and Kee, 2011). The MEAs are arranged in narrow strips that are supported on a chemically inert porous ceramic structure. The MEA width can be as small as a few millimeters. The electrochemically active materials are thin, with composite anode, dense electrolyte, and composite cathode being on the order of a few tens of microns thick. Fuel flows within the support structure, reaching the

anode via diffusive transport through the porous support structure. Air circulates on the outside the module, thus being available to the cathodes. Reaction products (e.g., H_2O and CO_2) counter-diffuse back through the support structure to the fuel channels. As illustrated in Figure 4, a thin reforming catalyst layer is applied on the inside of the support structure (Zhan and Barnett, 2005). This feature is intended to enable relatively high hydrocarbon concentrations in the fuel mixture.

Alternative SIS-SOFC architectures have been studied since the mid-1960s (Feduska and Isenberg, 1983; Isenberg, 1981; Minh, 1993). Initial efforts considered cells that were applied as rings to the exterior of cylindrical porous support tubes. Later designs considered planar cells that were applied to flat porous support structures (e.g., Figure 4). Mitsubishi Heavy Industries continues to develop SIS architectures on circular tubes (Tomida *et al.*, 2007), and Rolls-Royce is developing planar architectures (Agnew *et al.*, 2007; Gardner *et al.*, 2011). Rolls-Royce uses the name Integrated Planar Solid-Oxide Fuel Cell (IP-SOFC) to describe their design. Recently, Liu and colleagues have fabricated cone-shaped anode-supported SIS-SOFCs with good performance (Bai *et al.*, 2009, 2010).

1.2 Model formulation

Fuel cell models can be developed to meet a wide range of objectives. Achieving diverse objectives usually requires that the models incorporate significantly different levels of approximation. The design of SOFC stacks benefits from models that can predict gas flows through inlet and exhaust manifolds and flow distribution into multiple channel networks. Understanding and controlling thermal variations within the stack is another important stack-level design consideration. Models that focus on transport and chemistry at the microscale provide great value in assisting the optimization of MEA structures. Overall system performance depends upon the interaction of numerous balances of plant components (cf., Figure 1). Systems models require communication between system components, with the model of each component being computationally efficient. Real-time process-control algorithms can benefit from MPC that incorporates predictive physical knowledge. These models must be time accurate and be designed to represent available sensors and actuators. However, to be viable in real time with limited on-board computing capabilities, large physically based models must be substantially reduced.

The mathematical representation of the SOFCs must consider mass, energy, and charge transport processes (i.e., gas-phase species transport within the flow manifolds and the porous electrodes, electron transport within the electronic-conducting phases and the ion transport within the ionic-conducting phases, and energy transport within the cells) and

chemical reactions (i.e., thermal gas-phase chemical reactions with the flow manifolds, thermal catalytic chemistry within the electrodes, and electrochemical charge-transfer chemistry at the three-phase boundary (TPB) regions). The fluid flows within the manifolds for gas-phase species distribution are represented by Navier–Stokes equations (Goldin *et al.*, 2009). However, this chapter focuses on formulating mathematical models for the MEA structure.

2. CELL STRUCTURE

Based upon the stack structures shown in Figures 2–4, it is apparent that models of full stacks must deal with geometrical complexities and multiphysics interactions. For example, in planar stacks, the fluid mechanics in the inlet and exhaust manifold affects flow distribution to the channels and thus stack performance. Thermal balances are also important, usually seeking to maintain nearly uniform temperature throughout the entire stack. Although such three-dimensional models play an important role in stack development, the objective of this chapter is to focus on the cell and channel level.

As illustrated in Figure 5, the anode-supported MEA is composed of a relatively thick porous composite anode (e.g., 1 mm of Ni–YSZ), a thin

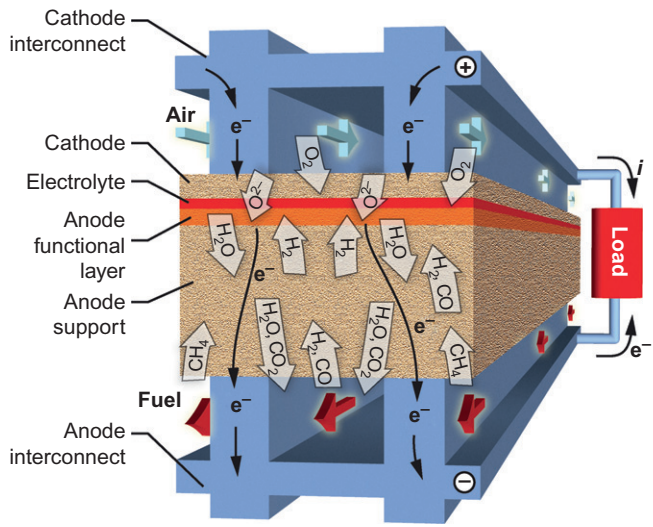

Figure 5 Details of the MEA and channel structure in a planar counterflow SOFC stack.

dense electrolyte membrane (e.g., 20 μm YSZ), and a thin porous composite cathode (e.g., 30 μm LSM–YSZ). The dense electrolyte transports only oxygen ions and is impermeable to any gas or electron transport. The MEA is sandwiched between bipolar[1] interconnect plates that also form fuel and air channels. The flow channels typically have dimensions (i.e., height and width) on the order of a millimeter but may be tens of centimeters long.

The composite anode and cathode are composed of three phases—electrode (electronic conducting), electrolyte (ion conducting), and pores (gas transport). The volume fraction for each phase is roughly 30%. The words ''anode'' and ''cathode'' are commonly used with two related, but different, meanings. The entire porous composite electrode structures can be called anodes and cathodes. However, for example, within a composite anode, the electron-conducting phase is called the anode phase and the ion-conducting phase is the electrolyte phase.

Composite electrodes are often fabricated with two layers—a thin functional layer (tens of microns) and a relatively thick support layer. Functional layers are designed with relatively small electrode and electrolyte particles to increase TPB length and thus facilitate charge-transfer chemistry. The outer support structures have larger particle and pore sizes, thus facilitating gas transport. Although particle and pore dimensions are small within the functional layers, the porosity in both functional and support layers is typically retained at around 30%.

Each of the three phases that comprise the electrodes (pore space, ion conductor, and electron conductor) must percolate through the electrode thickness, thus providing transport pathways for gases, ions, and electrons. Charge-transfer chemistry proceeds at the intersections between the three phases (i.e., TPB). Although a supporting anode structure can be relatively thick (i.e., order of millimeter), the charge transfer is usually accomplished within a few tens of microns around the electrolyte membrane (Zhu and Kee, 2008).

2.1 Composite cathode

The role of the cathode is to electrocatalytically reduce gas-phase molecular oxygen (O_2) to form oxygen ions (O^{2-}) within the electrolyte phase. The reaction can be represented globally as

$$\frac{1}{2}O_2(g) + 2e^-(c) \rightleftharpoons O^{2-}(e). \tag{1}$$

[1] When multiple cell are layered atop one another (e.g., Figure 2), the positive electrode of one layer becomes the negative electrode of the adjoining cell, hence, the designation bipolar.

This charge-transfer reaction occurs in close proximity to the TPB that are formed at the electrode–electrolyte interfaces that are also exposed to the gas. A charge-transfer reaction transfers electronic charge from one phase to another. Here, charge associated with the electrons in the electrode (cathode) phase is transferred to oxygen ions in the electrolyte phase. Each participating species is identified according to the phase in which it exists. That is, (g) represents the gas phase, (c) represents the cathode phase, and (e) represents the electrolyte phase. As discussed subsequently, the phase identification is especially important in evaluation of charge-transfer reaction rates.

2.2 Dense electrolyte membrane

The oxygen ions are conducted toward the dense electrolyte membrane via the connected (percolating) electrolyte particles within the composite cathode. The oxygen ions are then conducted through the dense electrolyte membrane to the electrolyte phase within the composite anode where they can catalytically electro-oxidize the fuel.

2.3 Composite anode

Assuming that hydrogen is the electrochemically active fuel, a global charge-transfer reaction may be stated as

$$\mathrm{H_2(g) + O^{2-}(e) \rightleftharpoons H_2O(g) + 2e^-(a)}. \tag{2}$$

In other words, gas-phase H_2 is oxidized by oxygen ions to deliver electrons into the anode (a) phase. The electrons are conducted through the percolating electron-conducting phase (e.g., Ni) of the composite electrode toward the anode current collector and then to an external circuit. After passing through the external circuit, the electrons return to the cathode where they serve to reduce molecular oxygen to oxygen ions (i.e., Reaction (1)). The electrochemical charge-transfer processes are usually confined to a region of less than 50 μm surrounding the dense electrolyte membrane.

It is known that CO can be electro-oxidized by O^{2-}, represented globally as

$$\mathrm{CO(g) + O^{2-}(e) \rightleftharpoons CO_2(g) + 2e^-(a)}. \tag{3}$$

However, the rates are slower by comparison with H_2 oxidation. Consequently, when hydrogen is available, it is reasonable to assume that hydrogen provides the dominant charge-transfer pathway (i.e., Reaction (2)).

In addition to its electrochemical function, the cermet anode support structure also facilitates hydrocarbon fuel reforming. It is often desirable to include low concentrations of methane (perhaps as much as 25%) in a reformed fuel stream. The reformed fuel that enters the SOFC may then be composed of H_2, CO, H_2O, CO_2, and CH_4. In addition to any H_2O and CO_2 in the entering fuel mixture, H_2O and CO_2 are also produced as a result of electrochemical oxidation. The Ni in the cermet anode serves as a reforming catalyst, using H_2O and CO_2 to convert CH_4 to H_2 and CO. The resulting hydrogen can participate in charge-transfer reactions (i.e., Reaction (2)). When H_2 is present, the CO is readily oxidized to CO_2 through the water-gas-shift reaction, producing yet more H_2. Table 1 lists some of the global reactions that may proceed on the catalyst surfaces. The last three reactions concern the formation of deleterious carbon deposits.

Because the reforming reactions are endothermic, the incorporation of some CH_4 in the fuel mixture can assist thermal management. Especially in large fuel cells, removing heat is an important consideration in maintaining a desired operating temperature. However, if the reforming chemistry proceeds too rapidly, then the entrance regions of fuel channels may become too cool, leading to deleterious large temperature gradients.

2.4 Electrode microstructure

Figure 6 is a particle-scale view of a planar MEA, emphasizing the structure of composite electrodes. In this idealized view, the composite electrodes are composed of percolating particles of electrolyte (e.g., YSZ) and electrode (e.g., Ni for the anode and LSM for the cathode). The electrolyte is assumed to be a pure oxygen-ion conductor, and the electrodes are presumed to be pure electron conductors. A typical composite electrode has phase volume fractions of approximately 33% each. The electrode and

Table 1 Possible global reactions for on-anode reforming processes

Name	Reaction	ΔH°_{298}(kJmol^{-1})
Steam reforming	$CH_4+H_2O \rightleftharpoons CO+3H_2$	206.1
Water-gas shift	$CO+H_2O \rightleftharpoons CO_2+H_2$	−41.2
Reverse Sabatier	$CH_4+2H_2O \rightleftharpoons CO_2+4H_2$	165.0
Dry reforming	$CH_4+CO_2 \rightleftharpoons 2CO+2H_2$	247.3
Methane cracking	$CH_4 \rightleftharpoons C(s)+2_2$	74.8
Boudouard	$2CO \rightleftharpoons C(s)+CO_2$	−173.3
CO reduction	$CO+H_2 \rightleftharpoons C(s)+H_2O$	−131.3

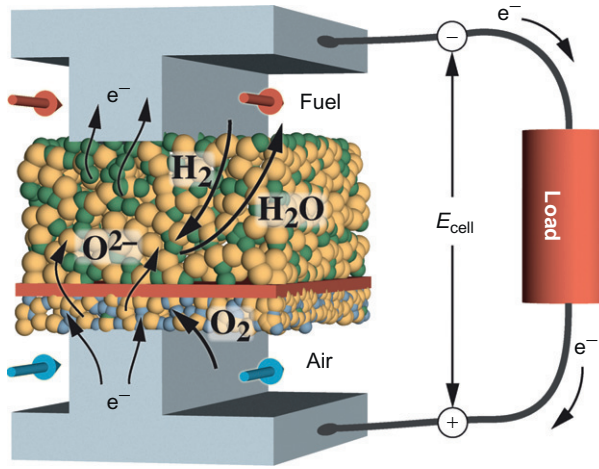

Figure 6 Section of a planar SOFC, showing an idealized MEA microstructure and connection with an external load.

electrolyte particle diameters, as well as the pore radii, are typically on the order of a fraction of a micron.

Although the idealized view (Figure 6) can be helpful in conceptualizing processes and models, it is important to recognize that actual electrodes may not be so easily represented. Figure 7 shows the microstructure of an actual MEA. The cathode is composed of a porous LSM–YSZ functional layer and a porous LSM current-collection layer. The anode is composed of a Ni–YSZ functional layer and a Ni–YSZ support structure.

As discussed subsequently, continuum-level modeling of ion, electron, and gas transport within the electrodes requires empirical relationships to represent effective conductivities. The empiricism can be approximated via modeling approaches including percolation theory or the explicit simulation of randomly packed spheres. It can also be established using experimental measurements.

3. GLOBAL ELECTROCHEMISTRY AND MEA MODELING

A fuel cell harnesses the potential energy associated with the oxidation of a fuel to do useful work. Unlike combustion, which primarily delivers heat, a fuel cell converts a significant fraction of the potential to electricity. Traditionally, the first step in modeling fuel-cell performance is to evaluate the reversible potential (Nernst potential, or equilibrium potential). At

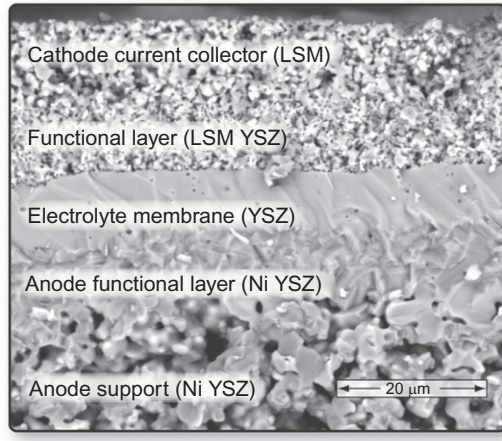

Figure 7 Scanning electron-microscope (SEM) image of an SOFC membrane-electrode assembly (Moyer *et al.*, 2011).

least for a fuel such as hydrogen, the Nernst potential can be represented in terms of the gas-phase composition in the fuel and oxidizer compartments, without specific knowledge of fundamental electrochemical processes.

3.1 Reversible potential

For reversible charge-transfer reactions (e.g., Reactions (1) and (2)) at equilibrium, the electrochemical potentials $\widetilde{\mu}_k$ are related as

$$\sum_k \nu_k \widetilde{\mu}_k = 0, \tag{4}$$

where ν_k are reaction stoichiometric coefficients. The species electrochemical potentials $\widetilde{\mu}_k$ are related to the chemical potentials μ_k and the electric potential Φ of participating phases as

$$\widetilde{\mu}_k = \mu_k + z_k F \Phi_k, \tag{5}$$

where F=96485.31 C mol^{-1} is Faraday's constant, z_k are the charges associated with the species, and Φ is the electric potential of the phase in which the species exists.

Consider first the global electrochemical oxygen reduction within the cathode (i.e., Reaction (1)). The electrochemical equilibrium can be expressed as

$$\frac{1}{2}\mu_{O_2,c} - 2F\Phi_c = \mu_{O^{2-},c} - 2F\Phi_{e,c}. \tag{6}$$

The gases are presumed to be electrically neutral (i.e., $z=0$), and the electrons have charge $z_{e^-}=-1$. The variable $\Phi_{e,c}$ represents the electrical potential of the electrolyte phase (oxygen ion-conducting phase) near a cathode TPB, and Φ_c is the electric potential of the cathode electronic-conducting phase. The electric-potential difference between the cathode and the electrolyte follows as

$$E_c^{eq} = \Phi_c - \Phi_{e,c} = \frac{1}{4F}\left(\mu_{O_2,c} - 2\mu_{O^{2-},c}\right). \tag{7}$$

An analogous analysis for electrochemical oxidation at the anode TPBs (i.e., Reaction (2)) yields

$$\mu_{H_2} + \mu_{O^{2-},a} - 2F\Phi_{e,a} = \mu_{H_2O} - 2F\Phi_a, \tag{8}$$

$$E_a^{eq} = \Phi_a - \Phi_{e,a} = \frac{1}{2F}\left(\mu_{H_2O,a} - \mu_{O^{2-},a} - \mu_{H_2,a}\right). \tag{9}$$

In this expression, $\Phi_{e,a}$ is the electric potential of the ion-conducting phase within the anode structure and Φ_a is the electric potential of the electron-conducting phase within the anode.

At open circuit (zero electrical current where $\mu_{O^{2-},c}=\mu_{O^{2-},a}$ and $\Phi_{e,c}=\Phi_{e,a}$), the reversible cell potential is evaluated by subtracting Equation (9) from Equation (7) to yield

$$E_{rev} = E_c^{eq} - E_a^{eq} = \frac{1}{2F}\left(\mu_{H_2,a} + \frac{1}{2}\mu_{O_2,c} - \mu_{H_2O,a}\right). \tag{10}$$

Note that the reversible cell potential depends only upon the gas-phase composition. Assuming ideal gases, the chemical potentials are evaluated as

$$\mu_k = \mu_k^\circ + RT\ln p_k, \tag{11}$$

where μ_k° are standard-state chemical potentials and p_k are partial pressures (in atm.). The reversible cell potential may be written in terms of the change in free energy for the global oxidation reaction $\left(\text{i.e., } H_2 + \tfrac{1}{2}O_2 \rightleftharpoons H_2O\right)$

$$E_{rev} = -\frac{\Delta G}{n_e F} = -\frac{\Delta G^\circ}{2F} - \frac{RT}{2F}\ln\frac{p_{H_2O,a}}{p_{H_2,a}p_{O_2,c}^{1/2}}, \tag{12}$$

where n_e is the number of electrons transferred by the global electrical reaction and

$$\Delta G^\circ = \mu^\circ{}_{H_2O,a} - \mu^\circ{}_{H_2,a} - \frac{1}{2}\mu^\circ{}_{O_2,c}. \tag{13}$$

The subscripts ''a'' and ''c'' on the partial pressures refer to the gases on the anode and cathode sides of the electrolyte membrane.

3.2 Polarization and overpotentials

Under ideal circumstances and at open circuit, the measured cell voltage should be the reversible cell potential $E_{cell}=E_{rev}=\Phi_c-\Phi_a$. However, when the cell is operating under load, the cell voltage E_{cell} is lower than the reversible potential E_{rev}. This difference is the result of *polarization*, which is defined to mean any departure from equilibrium or reversible electrical potential difference. The cell-operating voltage may be written as a function of current density i_e as (Zhu and Kee, 2003)

$$E_{cell} = E_{rev} - \eta_{conc,a}(i_e) - \eta_{act,a}(i_e) - \eta_{ohm}(i_e) - \left|\eta_{act,c}(i_e)\right| - \eta_{conc,c}(i_e), \tag{14}$$

where the various *overpotentials* are represented as η. Concentration overpotentials η_{conc} are the result of gas-transport resistance through the porous electrode structures, ohmic overpotentials η_{ohm} are caused primarily by resistance to ion transport through the electrolyte, and activation overpotentials η_{act} are the result of charge-transfer reactions. Because the electrode structures and relevant chemistries are different, the values of the overpotentials on the anode and cathode sides of the MEA are different.

Note that in Equation (14) the absolute value of the cathodic activation overpotential is used. As discussed subsequently, the activation overpotentials are usually evaluated from a Butler–Volmer equation. In this case, the activation overpotential is negative for cathodic reactions (i.e., reactions consuming electrons).

It is interesting to note that electrons are being delivered from the positive electrode (cathode) into the negative electrode (anode) within the MEA. Chemical energy associated with the charge-transfer chemistry must be expended to drive negative charge from the positive electrode into a negative electrode. As the current density increases, all the overpotentials must increase as well. In other words, as current density increases the system departs farther from equilibrium (i.e., increased polarization).

3.3 Ohmic overpotentials

The ionic conductivity for common ceramic electrolyte materials is usually expressed as

$$\sigma = \frac{\sigma_0}{T}\exp\left(-\frac{E_{el}}{RT}\right). \tag{15}$$

For YSZ, $\sigma_0 \approx 3.6\times10^5 \mathrm{S\,K\,cm^{-1}}$ and $E_{el} \approx 8\times10^4 \mathrm{J\,mol^{-1}}$ (Sasaki and Maier, 2000). It is evident that the conductivity varies strongly with temperature. The ohmic overpotential may be written as

$$\eta_{\text{ohm}} = i_{\text{e}} \frac{\ell_{\ell\text{ion}}}{\sigma}, \tag{16}$$

where ℓ_{ion} is the distance through which the oxygen ions must be transported. Modern YSZ electrolyte membranes are typically on the order of 10 μm thick. Ion transport through the ion-conducting particles within the electrode structure also contributes to the ohmic overpotenials. Moreover, electronic conduction within the electrode structures contributes to ohmic overpotential. However, for high electronic-conductivity materials such as Ni, the ohmic overpotentials are usually negligibly low.

3.4 Activation overpotentials

Charge-transfer reaction rates (e.g., Reactions (1) and (2)) are commonly represented in terms of the Butler–Volmer equation as

$$i_{\text{e}} = i_0(T, p_k)\left[\exp\left(\frac{\alpha_{\text{a}} F \eta_{\text{act}}}{RT}\right) - \exp\left(-\frac{\alpha_{\text{c}} F \eta_{\text{act}}}{RT}\right)\right], \tag{17}$$

where i_0 is the exchange current density and α_{a} and α_{c} are the anodic and cathodic symmetry factors. For a given current density, the activation overpotential is evaluated by inverting Equation (17).

The exchange current density represents the equal and opposite reaction rate under open-circuit conditions (i.e., no net current). Increasing catalyst activity and TPB length increases the exchange current density. The exchange current density i_0 is a relatively complex function of temperature and species partial pressures. There is a great deal of variability in the literature about how to evaluate exchange current density. Some papers even make the assumption that i_0 is constant. It is not uncommon for the species partial-pressure dependencies to be written in terms of the global reaction stoichiometry. Although this assumption is usually not correct, it is much better than assuming constant exchange current density. It is also common to use empirical reaction orders, meaning that the partial pressures of the reactants are raised to a power that is found to match measured performance. When the Butler–Volmer equation is derived from elementary charge-transfer kinetics, and making assumptions about rate-limiting steps, relatively complex partial-pressure dependencies can be found (Zhu *et al.*, 2005). In elementary charge-transfer reactions, the symmetry factors must sum to unity. However, for global charge-transfer reactions, the symmetry factors can be considerably different.

The current density represents the production (or consumption) of electrons. At the same time, although not explicitly evident in Equation (17), gas-phase and ionic species are also produced or consumed. Figure 8 shows graphs of the Butler–Volmer equation, plotting i/i_0 as a function of η_{act}. The plot on the right-hand side is in Tafel form, plotting

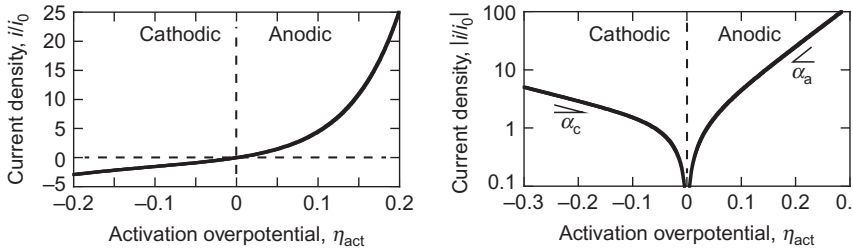

Figure 8 Illustration of the functional relationships between activation overpotential and current density in the Butler–Volmer equation. These graphs are produced using T=800°C, α_a=3/2, and α_c=1/2.

the logarithm of $|i/i_0|$. The Butler–Volmer equation represents a reversible reaction, which means that the net current is the difference between anodic (i.e., producing electrons) and cathodic (i.e., consuming electrons) rates. The first term in Equation (17) represents the anodic rate, and the second term represents cathodic rate. A positive activation overpotential produces net anodic current and a negative activation overpotential produces net cathodic current. Within the anode of a fuel cell, the net charge-transfer rates are anodic (i.e., Reaction (2) is producing electrons) and thus $\eta_{act,a}>0$. Within the cathode of a fuel cell, the net charge-transfer rates are cathodic (i.e., Reaction (1) is consuming electrons) and thus $\eta_{act,c}<0$. Plotted on semilog axes (right-hand side of Figure 8), the so-called Tafel slopes approach constants that are proportional to the symmetry factors α.

3.5 Concentration overpotentials

As discussed above, a reversible potential can be evaluated based upon gas-phase partial pressures in the fuel and air compartments. When a cell is under load (i.e., delivering current), the gas-phase concentrations in the fuel and air channels are different than they are in the proximity of the dense electrolyte where the charge-transfer chemistry proceeds. The difference in the reversible potentials evaluated in the flow channels and across the dense electrolyte membrane are the concentration overpotentials.

With nonreactive gas transport within the electrode (e.g., only H_2 and H_2O), using the concentration overpotential can be convenient. However, when there is significant reforming chemistry within the anode structure, the notion of concentration overpotential tends to be not particularly useful. As discussed subsequently, with channel models that solve the reactive porous-media problem within the electrodes,

there is no explicit need to involve concentration overpotentials as in Equation (14).

4. FUNDAMENTAL ELECTROCHEMISTRY

Although the traditional approach to representing charge-transfer chemistry via Butler–Volmer formulation and activation overpotentials is widely practiced and generally appealing, it has inherent limitations. Representing parallel charge-transfer pathways in terms of a Nernst potential and activation overpotentials requires significant limiting assumptions. For example, if gas-phase H_2 and CO are not in chemical equilibrium, there is no unambiguous way to establish a Nernst potential. An alternative is to represent all chemical reactions (thermal and electrochemical) as elementary reversible reactions whose rates are represented through fundamental mass-action kinetics. Microscopic reversibility is assured through thermodynamically consistent properties for all participating species. Open-circuit potential is an outcome of the model, not a starting point. There are many potential benefits associated with the elementary approach. For example, parallel charge-transfer pathways can be represented unambiguously.

Goodwin was the first to propose the direct incorporation of elementary charge-transfer reaction mechanisms into SOFC models (Goodwin, 2005). This proposal followed related efforts in which a set of charge-transfer reactions could be reduced to a modified Butler–Volmer form using some simplifying assumptions (Kee *et al.*, 2005; Zhu *et al.*, 2005). Bessler and others have built on the approach of incorporating elementary charge-transfer reactions and have explored alternative charge-transfer pathways (Bessler *et al.*, 2007a,b; DeCaluwe *et al.*, 2008; Vogler *et al.*, 2009). Recent efforts have incorporated parallel H_2 and CO charge-transfer pathways (Moyer *et al.*, 2011; Yurkiv *et al.*, 2011).

The elementary approach to represent the complex electrochemical charge-transfer processes involves the electric potentials and species activities in multiple phases (i.e., gas-phase species, surface adsorbates, and bulk species in the solid materials). In addition to current density alone (i.e., the production and consumption of electrons), the elementary approach must also be concerned with the kinetic rates of progress for many participating species. Figure 9 illustrates a possible elementary charge-transfer mechanism at a Ni–YSZ particle interface. This mechanism accommodates the possibility of charge transfer via competitive H_2 and CO pathways. Heterogeneous chemistry on the Ni and YSZ surfaces does not involve charge-transfer reactions, but it is responsible for producing the species that participate in the

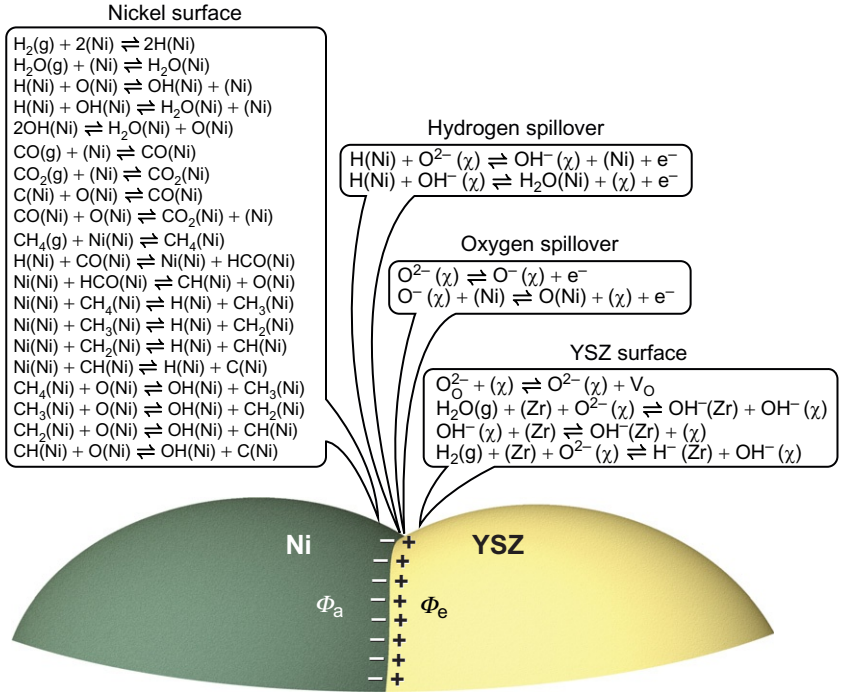

Figure 9 Chemical reactions on a Ni electrode surface, an YSZ electrolyte surface, and charge-transfer reactions at the particle interface.

electrochemistry. This mechanism is developed assuming two surface site types (Zr and χ) on the YSZ surface (Goodwin *et al.*, 2009). The details of the thermodynamic properties and chemical kinetic rate parameters are documented in Moyer *et al.* (2011).

Chemical reactions, including charge-transfer reactions, can be written generally as

$$\sum_{k=1}^{K} \nu'_{ki} \Lambda_k^{z_k} \rightleftharpoons \sum_{k=1}^{K} \nu''_{ki} \Lambda_k^{z_k}, \tag{18}$$

where $\Lambda_k^{z_k}$ is the chemical symbol of the kth species with charge z_k. The forward and reverse stoichiometric coefficients for the kth species in the ith reaction are ν'_{ki} and ν''_{ki}, respectively. In this setting, electrons are considered as species. The rates of progress for the ith reaction q_i are represented as

$$q_i = k_{ai} \prod_{k=1}^{K} C_k^{\nu'_{ki}} - k_{ci} \prod_{k=1}^{K} C_k^{\nu''_{ki}}, \tag{19}$$

where C_k represent the activities of participating species. The activity of a gas-phase species is its molar concentration $[X_k]$. The activity of a surface-adsorbed species is the surface coverage $\Gamma_m \theta_{k,m}$, where $\theta_{k,m}$ is the site fraction for species k on the surface of site-type m and Γ_m is the total available surface-site density for site-type m. The molar production rate for kth species resulting from the ith reaction $\dot{s}_{ki}$ is written as

$$\dot{s}_{ki} = (\nu''_{ki} - \nu'_{ki}) q_i = \nu_{ki} q_i, \tag{20}$$

where the net stoichiometric coefficients are defined as $\nu_{ki} \equiv \nu''_{ki} - \nu'_{ki}$.

Anodic (i.e., producing electrons) and cathodic (i.e., consuming electrons) rate expressions may be written as

$$k_{ai} = k_{ai}^t \exp\left[-\beta_{ai} \frac{F}{RT} \sum_{k=1}^{K} \nu_{ki} z_k \Phi_k \right], \tag{21}$$

$$k_{ci} = k_{ci}^t \exp\left[+\beta_{ci} \frac{F}{RT} \sum_{k=1}^{K} \nu_{ki} z_k \Phi_k \right]. \tag{22}$$

For elementary charge-transfer reactions (i.e., transferring a single electron), the anodic and cathodic symmetry factors are constrained as $\beta_{ai} + \beta_{ci} = 1$.[2]

The rates of charge-transfer reactions depend upon the electric potentials Φ_m of m participating phases. For example, a reaction that transfers charge from an YSZ phase to a Ni phase in a composite electrode depends upon the difference in electric potential between the YSZ and Ni phases. It is assumed that every charged species is at the electric potential of the phase in which it resides. Thus, as written in Equations (21) and (22), it is convenient to associate the electric potentials with species k. If all species in a reaction are at the same electric potential, or if all participating species are uncharged, the exponential factors in Equations (21) and (22) become unity. In this case, the rate expressions revert to those for purely thermal reactions.

The thermal component of the anodic (forward) rate expression is written in modified Arrhenius form as

$$k_{ai}^t = A_i T^{n_i} \exp\left(-\frac{E_i}{RT} \right), \tag{23}$$

where E_i represents an activation energy, A_i a pre-exponential factor, and n_i a temperature exponent. To ensure microscopic reversibility the

[2] Note that in global reactions, such as represented by the Butler–Volmer equation (Equation (17)), the symmetry factors are represented as α_a and α_c. In general, $\alpha_a + \alpha_c \neq 1$.

thermal component of the cathodic (reverse) rate is related to the forward rate via the reaction's equilibrium constant K_i as

$$K_i = \frac{k_{ai}^{t}}{k_{ci}^{t}} = \exp\left(-\frac{\Delta G^{\circ}}{RT}\right), \tag{24}$$

where ΔG° is the change in standard-state free energy for the reaction. Evaluating ΔG°, and hence the equilibrium constant, requires consistent thermochemical properties for all species. Unlike evaluating gas-phase thermodynamic properties, however, evaluating such thermodynamic properties for the surface adsorbates and bulk species is often difficult.

The net species production rate $\dot{s}_k$ resulting from all of reactions I involving species k can be written as

$$\dot{s}_k = \sum_{i=1}^{I} \dot{s}_{ki} \Psi_{ik}, \tag{25}$$

where Ψ_{ik} are microstructural factors that depend upon the reaction and the species involved (Zhu and Kee, 2008). Because charge-transfer reactions typically proceed at three-phase interfaces between electrode, electrolyte, and gas phases, the species production rates $\dot{s}_{ki}$ are usually written in terms of three-phase-boundary length ($\mathrm{mol\,cm^{-1}\,s^{-1}}$). Such reactions usually involve species on different surface phases, electrons and ions within different phases, and possibly gas-phase species. For both gas-phase species and electrons, $\Psi_{ik}=\lambda^{\mathrm{V}}_{\mathrm{TPB},i}$ is the three-phase-boundary length per unit volume of porous electrode. For surface species, $\Psi_{ik}=\lambda^{\mathrm{V}}_{\mathrm{TPB},i}/A_{\mathrm{s}}$ is the ratio of the specific TPB length and the specific area of the surface on which the species exists. The total charge-transfer rate per unit volume from all the electrochemical reactions can be represented as

$$\dot{s}_{\mathrm{e}} = \sum_{i=1}^{I} \lambda^{\mathrm{V}}_{\mathrm{TPB},i} i_{\mathrm{e},i}, \tag{26}$$

where $i_{\mathrm{e},i}=n_{\mathrm{e},i}Fq_i$ is the current density per unit length resulting from the ith electrochemical charge-transfer reaction and $n_{\mathrm{e},i}$ is the number of electrons transferred.

To assist the physical understanding of electric-potential differences on charge-transfer rates, consider the following reaction that is part of the hydrogen-spillover charge-transfer mechanism:

$$\mathrm{H(Ni)} + \mathrm{OH^-}(\chi) \rightleftharpoons \mathrm{H_2O(Ni)} + (\chi) + \mathrm{e^-(Ni)}. \tag{27}$$

Two surface sites are involved: One is the Ni surface and the other is a χ site on the YSZ surface (Goodwin *et al.*, 2009). As illustrated in Figure 9, the Ni anode is at electric potential Φ_{a} and the YSZ electrolyte is at electric potential Φ_{e}.

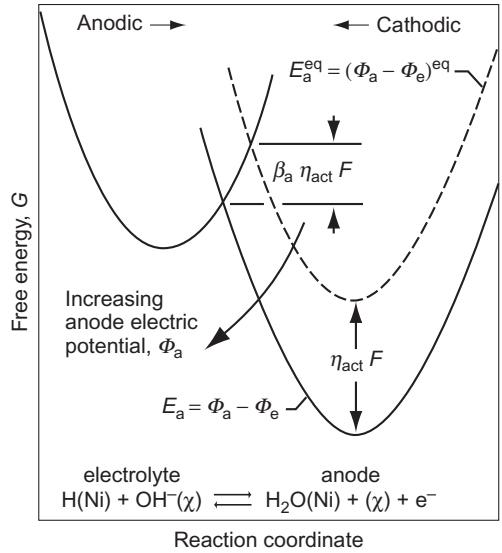

Figure 10 Potential-energy surfaces to assist visualizing the effect of electric-potential difference on charge-transfer reaction rates.

Figure 10 represents potential-energy surfaces as functions of a reaction coordinate. The potential-energy surface on the left represents the reactants and the one on the right represents the products. The electric-potential difference between the Ni (i.e., the anode) and the YSZ (i.e., the electrolyte) is written as $E_a = \Phi_a - \Phi_e$. The equilibrium electric-potential difference E_a^{eq} is the electric-potential difference at which the reaction proceeds at equal and opposite rates in the anodic and cathodic directions (illustrated as the dashed line). A cusp-like transition state forms a potential-energy barrier between the reactant and product states.

When proceeding in the anodic (forward) direction, the charge-transfer reaction illustrated in Figure 10 is delivering electrons into the anode, which is at a lower electric potential than the electrode. As the electric potential of the anode is increased relative to the electrolyte (i.e., E_a increases), the barrier to the electron transfer is decreased. The negatively charged electron is naturally repelled from the negative electrode. Some of the chemical energy stored in the reactants is converted to electricity as electrons are delivered into the anode (i.e., the conduction band of the Ni). When the electric potential of the anode is increased (i.e., becomes less negative), the barrier to charge transfer decreases. The symmetry factors β (Equations (21) and (22)) are related to the magnitudes of the slopes of the potential-energy surfaces at their crossing point. Because the slopes are

typically similar, the symmetry factors for elementary reactions are usually near $\beta \approx 1/2$. More detailed discussion on formulating charge-transfer rates can be found in Kee *et al.* (2005) and in textbooks on electrochemistry (Bard and Faulkner, 2000; Bockris *et al.*, 2000).

The equilibrium electric-potential difference for Reaction (27) can be evaluated as

$$E_a^{eq} = \left(\Phi_{Ni} - \Phi_\chi\right)^{eq} = \frac{1}{F}\left(\mu_{H_2O(Ni)} + \mu_{(\chi)} - \mu_{OH^-(\chi)} - \mu_{H(Ni)}\right). \tag{28}$$

Quantitatively evaluating E_a^{eq} requires evaluating the chemical potentials, which can be difficult for the surface adsorbates for which data are not readily available. Goodwin *et al.* (2009) discuss the evaluation of needed thermodynamic properties.

The difference between E_a and E_a^{eq} is activation overpotential: $\eta_{act} = E_a - E_a^{eq}$. As illustrated in Figure 10 the product of the activation overpotential and Faraday's constant (i.e., $\eta_{act}F$) represents the shift in the potential-energy surface upon a change in the electric-potential difference between participating phases. The barrier height to the forward (anodic) reaction changes by a fraction β_a of the potential-energy surface shift.

4.1 Elementary reaction in Butler–Volmer form

For an individual charge-transfer reaction, there is a direct relationship between the charge-transfer rate as expressed in the form of an elementary reaction and as expressed in Butler–Volmer form. As an example, consider Reaction (27). Assuming elementary charge-transfer chemistry, the Faradic current density i_e can be evaluated as

$$i_e = -F\lambda_{TPB}^V\left(k_a[H(Ni)][OH^-(\chi)] - k_c[H_2O(Ni)][(\chi)]\right), \tag{29}$$

where λ_{TPB}^V is the specific TPB length. The anodic and cathodic electrochemical rate expressions can formally be expressed as

$$k_a = k_a^t \exp\left(+\frac{\beta_a F E_a}{RT}\right), \tag{30}$$

$$k_c = k_c^t \exp\left(-\frac{\beta_c F E_a}{RT}\right). \tag{31}$$

Because the reaction is elementary, the symmetric factors β_a and β_c satisfy $\beta_a + \beta_c = 1$. The equilibrium electric-potential difference E_a^{eq} can be represented as,

$$E_a^{eq} = \frac{RT}{F}\ln\left(\frac{k_c^t}{k_a^t}\frac{[H_2O(Ni)][(\chi)]}{[H(Ni)][OH^-(\chi)]}\right). \tag{32}$$

In terms of the activation overpotential $\eta_{act} = E_a - E_a^{eq}$, the current density i_e can be rewritten in Butler–Volmer formulation as,

$$i_e = i_e^0\left[\exp\left(\frac{\beta_a F\eta_{act}}{RT}\right) - \exp\left(-\frac{\beta_c F\eta_{act}}{RT}\right)\right], \tag{33}$$

where the exchange current density i_e^0 has the following form,

$$i_e^0 = -F\lambda_{TPB}^V\left(k_a^t\right)^{\beta_c}\left(k_c^t\right)^{\beta_a}[\mathrm{H(Ni)}]^{\beta_c}[\mathrm{OH}^-(\chi)]^{\beta_c}[\mathrm{H_2O(Ni)}]^{\beta_a}[(\chi)]^{\beta_a}. \tag{34}$$

Notice that the apparent reaction orders in Butler–Volmer form are different from the reaction orders in elementary form (i.e., Equation (29)). Bessler *et al*. provide a physical interpretation of this apparent change in reaction order (Bessler *et al*., 2007b).

4.2 Multiple reaction steps in Butler–Volmer form

Although one may anticipate that the partial-pressure dependencies for the exchange current densities follow the stoichiometry of the global charge-transfer reactions (i.e., Reactions (1) and (2)), this is usually not the case. For a given charge-transfer reaction mechanism, the functional form of the exchange current density and global symmetry factors can be derived by assuming one elementary reaction is rate limiting and that all other reactions are partially equilibrated. At the anode side, hydrogen is assumed to be the only electrochemically active fuel species, even though the fuel stream may consist of hydrocarbons and carbon monoxide. And at the cathode side, only oxygen is considered to be the electrochemically active. Based upon an elementary charge-transfer reaction mechanism for the electrochemical oxidation of hydrogen at the anode and assumptions about the rate-limiting steps, expressions for the exchange current densities can be developed (Zhu *et al*., 2005) as

$$i_{0,\mathrm{H_2}} = i^*_{\mathrm{H_2}}\frac{\left(p_{\mathrm{H_2}}/p^*_{\mathrm{H_2}}\right)^{(1-\alpha_a/2)}\left(p_{\mathrm{H_2O}}\right)^{\alpha_a/2}}{1+\left(p_{\mathrm{H_2}}/p^*_{\mathrm{H_2}}\right)^{1/2}}, \tag{35}$$

where $i_{\mathrm{H_2}}{}^*$ and $p_{\mathrm{H_2}}{}^*$ are only functions of temperature. The global symmetry factors for the electrochemical oxidation of hydrogen are assumed to be α_a=1.5 and α_c=0.5. An analogous expression for electrochemical reduction of oxygen at the cathode is found to be

$$i_{0,\mathrm{O_2}} = i^*_{\mathrm{O_2}}\frac{\left(p_{\mathrm{O_2}}/p^*_{\mathrm{O_2}}\right)^{\alpha_a/2}}{1+\left(p_{\mathrm{O_2}}/p^*_{\mathrm{O_2}}\right)^{1/2}}. \tag{36}$$

The parameter $p^*_{\mathrm{O_2}}$ depends upon O_2 adsorption/desorption rates. Global symmetry factors for the oxygen reduction are taken to be α_a=0.5 and α_c=0.5. In addition to composition dependencies, the exchange current densities i^* depend on temperature as

$$i^* = i^*_{\text{ref}} \exp\left[-\frac{E}{R}\left(\frac{1}{T} - \frac{1}{T_{\text{ref}}}\right)\right]. \tag{37}$$

The parameter i^*_{ref} is the nominal exchange current density at the reference temperature T_{ref}, E is an activation energy, and R is the gas constant.

5. SPATIALLY RESOLVED MEA MODEL

The MEA must be designed to accomplish several physical and chemical functions, including gas transport through the pore volume of composite electrodes, ion and electron transport through the solid phases, heat generation and transport, catalytic reforming chemistry, and electrochemical charge transfer. Because the relative contributions of these functions vary spatially throughout the MEA, it is important to develop models that can predict the spatial variations, and hence the resulting fuel-cell performance.

5.1 Gas-phase transport

Reacting gas-phase species transport through the porous electrodes is represented by species and overall mass-conservation equations as

$$\frac{\partial\left(\phi_g \rho Y_k\right)}{\partial t} + \nabla\cdot\mathbf{j}_k = W_k \underline{S}_k, \tag{38}$$

$$\frac{\partial\left(\phi_g \rho\right)}{\partial t} + \sum_{k=1}^{K_g} \nabla\cdot\mathbf{j}_k = \sum_{k=1}^{K_g} W_k \underline{S}_k, \tag{39}$$

where ϕ_g is the porosity; ρ is the gas-phase density; and the gas-phase mass fractions, molecular weights, and mass fluxes are represented by Y_k, W_k, and $\mathbf{j}_k$, respectively. The gas-phase species mass fluxes within the porous media are primarily the result of molecular diffusion processes, with pressure-driven flow (Darcy) being a small contributor. However, because the pore dimensions can be on the order of the gas-phase mean-free path lengths, Knudsen diffusion is relevant. Vural *et al.* have reviewed and evaluated several alternative models to represent gas-phase transport in SOFC electrodes (Vural *et al.*, 2010).

The model presented here determines mass fluxes $\mathbf{j}_k$ using the Dusty-Gas model (DGM) (Mason and Malinauskas, 1983; Zhu *et al.*, 2005). The DGM is an implicit relationship among the gas-phase species molar fluxes $\mathbf{J}_k$, molar concentrations $[X_k]$, concentration gradients, and the pressure p gradient as

$$\sum_{\ell \neq k} \frac{[X_\ell]\mathbf{J}_k - [X_k]\mathbf{J}_\ell}{[X_\mathrm{T}]D^\mathrm{e}_{k\ell}} + \frac{\mathbf{J}_k}{D^\mathrm{e}_{k,\mathrm{Kn}}} = -\boldsymbol{\nabla}[X_k] - \frac{[X_k]}{D^\mathrm{e}_{k,\mathrm{Kn}}}\frac{B_\mathrm{g}}{\mu}\boldsymbol{\nabla}p, \tag{40}$$

where μ is the mixture viscosity and $[X_\mathrm{T}]=p/RT$ is the total molar concentration. The mass fluxes $\mathbf{j}_k$ are related to the molar fluxes $\mathbf{J}_k$ as $\mathbf{j}_k=W_k\mathbf{J}_k$. $D^\mathrm{e}_{k\ell.}$ and $D^\mathrm{e}_{k,\mathrm{Kn}}$ are the effective ordinary and Knudsen diffusion coefficients, respectively. Knudsen diffusion represents mass transport assisted by gas-surface collisions. The Knudsen diffusion coefficients depend upon the porous-media microstructure, including porosity, average pore radius r_p, and tortuosity τ_g. The effective binary and Knudsen diffusion coefficients $D^\mathrm{e}_{k\ell}$ and $D^\mathrm{e}_{k,\mathrm{Kn}}$ can be evaluated as

$$D^\mathrm{e}_{k\ell} = \frac{\phi_\mathrm{g}}{\tau_\mathrm{g}}D_{k\ell}, \quad D^\mathrm{e}_{k,\mathrm{Kn}} = \frac{2}{3}\frac{r_\mathrm{p}\phi_\mathrm{g}}{\tau_\mathrm{g}}\sqrt{\frac{8RT}{\pi W_k}}. \tag{41}$$

The ordinary multicomponent diffusion coefficients $D_{k\ell}$ and the mixture viscosities μ are determined from kinetic theory (Kee *et al.*, 2003). The permeability B_g can be evaluated from the Kozeny–Carman relationship as

$$B_\mathrm{g} = \frac{\phi_\mathrm{g}^3 d_\mathrm{p}^2}{72\tau_\mathrm{g}\left(1-\phi_\mathrm{g}\right)^2}, \tag{42}$$

where d_p is the particle diameter. Details about the DGM and the computational implementation are reported by Zhu *et al.* (2005).

Under typical SOFC conditions, porous-media transport is dominated by diffusive processes (i.e., ordinary and Knudsen diffusion). The production and consumption of gas-phase species via heterogeneous chemistry within the porous electrode can produce pressure variations across the electrode structure. However, the mass transport associated with relatively small pressure differences (order 1000 Pa or less) contributes very little to the net mass transport. Porosity is relatively easy to measure, and effective particle diameters and pore radii can be reasonably estimated from microscopic images of the electrodes. However, transport depends strongly on tortuosity, which is difficult to measure. Thus, tortuosity is often used as an empirical parameter that is adjusted to fit transport measurements.

The molar production rates of gas-phase species due to heterogeneous thermal catalytic chemistry and electrochemical charge-transfer reactions are represented by $\dot{s}_k$. Because the pore size within an electrode is usually comparable to the molecular mean-free path length, the probability for gas–gas collisions is relatively low. Moreover, the temperatures are relatively low (i.e., compared to combustion temperatures). Thus, the homogeneous gas-phase kinetics is negligible. The production rates $\dot{s}_k$ are functions of temperature, gas composition, surface-species coverages,

and electric-potential differences between the electrode and electrolyte phases. In addition to gas-phase species, the chemistry also depends on surface-adsorbed species. The temporal variations of site coverages θ_k of surface-adsorbed species are represented as

$$\frac{\mathrm{d}\theta_k}{\mathrm{d}t} = \frac{\dot{s}_k}{\Gamma}, \quad k = 1, \ldots, K_\mathrm{s}, \tag{43}$$

where Γ is available site density and K_s is the number of surface-adsorbed species. At steady state, the net production rates of surface species vanish (i.e., $\dot{s}_k$=0).

5.2 Ion and electron transport

Fuel-cell performance depends upon the interactions of at least three electric-potential fields (i.e., Φ_a within the anode's electron-conducting phase, Φ_c within the cathode's electron-conducting phase, and Φ_e within the electrolyte phase). For mixed-conducting composite electrodes (e.g., Figure 6), there is electrolyte phase in both the anode and the cathode structures. For example, in a Ni–YSZ | YSZ | LSM–YSZ structure, YSZ is the electrolyte phase throughout the MEA. The three electric-potential fields are established to satisfy charge conservation as

$$\frac{\partial q_\mathrm{e}}{\partial t} = \boldsymbol{\nabla}\cdot\left(\sigma_\mathrm{e}^\mathrm{e}\boldsymbol{\nabla}\Phi_\mathrm{e}\right) - \boldsymbol{\nabla}\cdot\mathbf{i}_\mathrm{e,c} - \begin{cases} \underline{s}_\mathrm{a,e} & \text{within anode} \\ 0 & \text{within electrolyte} \\ \underline{s}_\mathrm{c,e} & \text{within cathode} \end{cases}, \tag{44}$$

$$\frac{\partial q_\mathrm{a}}{\partial t} = \boldsymbol{\nabla}\cdot\left(\sigma_\mathrm{a}^\mathrm{e}\boldsymbol{\nabla}\Phi_\mathrm{a}\right) - \boldsymbol{\nabla}\cdot\mathbf{i}_\mathrm{a,c} + \underline{s}_\mathrm{a,c} \quad \text{within anode}, \tag{45}$$

$$\frac{\partial q_\mathrm{c}}{\partial t} = \boldsymbol{\nabla}\cdot\left(\sigma_\mathrm{c}^\mathrm{e}\boldsymbol{\nabla}\Phi_\mathrm{c}\right) - \boldsymbol{\nabla}\cdot\mathbf{i}_\mathrm{c,c} + \underline{s}_\mathrm{c,e} \quad \text{within cathode}. \tag{46}$$

In these equations, $\sigma_\mathrm{a}^\mathrm{e}$ and $\sigma_\mathrm{c}^\mathrm{e}$ are the effective conductivities of the electron-conducting phases in the anode and the cathode. The effective ion conductivities for the ion-conducting phase are $\sigma_\mathrm{e}^\mathrm{e}$. Note again that there are typically ion-conducting phases in the anode and cathode structures as well as in the dense electrolyte membrane.

5.3 Energy transport

Because the pore spaces are small and the gas-phase heat capacity is small, it is reasonable to assume that the gas and solid phases within the electrode structures share a common, but spatially varying, local temperature T. Considering heat transport due to thermal conduction and gas-phase species diffusion, as well as Joule heating and the thermal

consequences of chemical and electrochemical reactions, the energy balance within the porous electrodes can be written as

$$\frac{\partial E_\mathrm{t}}{\partial t} + \boldsymbol{\nabla}\cdot\mathbf{q}_\mathrm{t} = -\dot{s}_\mathrm{e}E^\mathrm{eq} + \dot{s}_\mathrm{e}\eta_\mathrm{act} + \sum_m \frac{\mathbf{i}_m\cdot\mathbf{i}_m}{\sigma_m^\mathrm{e}}. \tag{47}$$

In this equation, η_act is the local activation overpotential for the charge-transfer process, $\dot{s}_\mathrm{e}$ is the local charge-transfer rate between the electrode and electrolyte phases, and E^eq the local equilibrium electric-potential difference (i.e., $\eta_\mathrm{act}=\eta_\mathrm{act,a}$, $\dot{s}_\mathrm{e}=\dot{s}_\mathrm{a,e}$, and $E^\mathrm{eq}=E_\mathrm{a}^\mathrm{eq}$ in the anode; and $\eta_\mathrm{act}=\eta_\mathrm{act,c}$, $\dot{s}_\mathrm{e}=\dot{s}_\mathrm{c,e}$, and $E^\mathrm{eq}=E_\mathrm{c}^\mathrm{eq}$ in the cathode). The total internal energy E_t, including gas and solid phases, is expressed as

$$E_\mathrm{t} = \phi_\mathrm{g}\rho e + \left(1-\phi_\mathrm{g}\right)\rho_\mathrm{s}c_\mathrm{s}T, \tag{48}$$

where e is the gas-phase internal energy and ρ_s and c_s are the density and heat capacity of the solid phase, respectively. The heat flux due to thermal conduction and species diffusion can be represented as

$$\mathbf{q}_\mathrm{t} = -\lambda\boldsymbol{\nabla}T + \sum_k \mathbf{j}_k h_k \tag{49}$$

where h_k are gas-phase species enthalpies and λ is the effective thermal conductivity, representing an average of all phases.

The term $\dot{s}_\mathrm{e}E^\mathrm{eq}$ in Equation (47) represents the ideal electric power resulting from the charge-transfer reactions and should be subtracted from the overall energy-conservation equation. In other words, the energy that leaves the system as electricity does not contribute to the thermal balance. However, a portion of the generated electric power must be used to overcome internal inefficiencies, which manifests itself as heat. The activation overpotential losses associated with the charge-transfer reactions are written as $\eta_\mathrm{act}\ \dot{s}_\mathrm{e}$. The ohmic losses for the ion and electron transport through the electrodes are written as $\sum_m \mathbf{i}_m\cdot\mathbf{i}_m/\sigma_m^\mathrm{e}$.

Because there are no gaseous species and also no chemical and electrochemical reactions within the dense electrolyte, its energy equation is represented more simply as

$$\frac{\partial(\rho_\mathrm{s}c_\mathrm{s}T)}{\partial t} = \boldsymbol{\nabla}\cdot\lambda\boldsymbol{\nabla}T + \frac{\mathbf{i}_\mathrm{el}\cdot\mathbf{i}_\mathrm{el}}{\sigma_\mathrm{el}^\mathrm{e}} \tag{50}$$

where $\mathbf{i}_\mathrm{el}$ is the current density and $\sigma_\mathrm{el}^\mathrm{e}$ is the ion conductivity.

5.4 Effective transport properties

Although the MEA may have a complex three-dimensional microstructure (e.g., Figure 7), Equations (44)–(46) are written as continuum partial differential equations with effective conductivities. The effective conductivities that appear in Equations (44)–(46) are usually much smaller than the

conductivities of the materials from which the composite is fabricated. Thus, it is necessary to establish quantitative relationships between intrinsic material properties and the effective properties for particular microstructures.

Percolation theory provides one possible approach (Chan and Xia, 2001; Chan *et al.*, 2004, 2009; Costamagna *et al.*, 1998; Nam and Jeon, 2006). Although based upon major simplifying assumptions about randomly packed overlapping spheres, the percolation theory leads to relatively simple analytical expressions for effective properties. Another approach is to computationally solve three-dimensional transport problems through representative random arrangements of particles. The electrode microstructure is approximated with spherical particles using alternative packing algorithms (Metcalfe *et al.*, 2009; Rüger *et al.*, 2009; Sanyal *et al.*, 2010; Shearing *et al.*, 2009). This approach also relies on significant assumptions about particle shapes and packing configurations, both of which are difficult to validate quantitatively.

Another approach is to model transport through small samples of the actual three-dimensional structures as reconstructed from microscopic experiments (Gunda *et al.*, 2011). Beginning with Wilson *et al.* (2006), several groups have developed focused-ion-beam-scanning-electron-microscope (FIB-SEM) experiments to reconstruct composite electrodes (Gostovic *et al.*, 2007; Iwai *et al.*, 2010; Rüger *et al.*, 2009; Shearing *et al.*, 2009; Smith *et al.*, 2009; Wilson *et al.*, 2009a,b, 2010). Izzo *et al.* have developed similar electrode reconstructions of actual electrodes using X-ray tomography (Grew *et al.*, 2009; Izzo *et al.*, 2008).

5.5 Thermal catalytic chemistry

As shown in Figure 9, thermal heterogeneous chemistry (i.e., not charge-transfer electrochemistry) proceeds on the Ni and YSZ surfaces. In addition to its role in the electrochemical charge-transfer process, this heterogeneous chemistry, especially on the Ni surface, also represents fuel reforming and water-gas-shift processes. In other words, these detailed reaction mechanisms are a more-fundamental alternative to the global processes as stated in Table 1.

Although certainly more complex than a few global reactions, the detailed reaction mechanisms provide some significant advantages. Detailed mechanisms can represent essentially all combinations of steam reforming, dry reforming, partial oxidation, and autothermal reforming. The majority of traditional SOFC modeling literature uses only two global reactions (i.e., steam reforming and water-gas shift; Table 1). However, such an approach is incapable of modeling the reforming effects of CO_2 or O_2 in the fuel stream, both of which occur commonly on practice. Detailed catalytic reaction mechanisms on Ni surfaces have

been developed and validated using a range of experiments (Hecht *et al.*, 2005; Janardhanan and Deutschmann, 2006; Zhu *et al.*, 2005). However, because this topic is covered in another chapter of this book, the development of catalytic reaction mechanisms is not discussed further here.

A major concern in reforming chemistry is the formation and deposition of carbon deposits that deactivate the reforming catalyst, especially Ni. Deposit formation may be the result of gas-phase pyrolysis, leading to molecular-weight growth and ultimately polynuclear aromatic hydrocarbon deposits (Gupta *et al.*, 2006a). Deposit formation may also be caused by heterogeneous chemistry, leading to direct graphitic-like carbon deposits (i.e., coking) on the catalyst (McIntosh *et al.*, 2004). In the later case, the gas-phase formation of small olefins (e.g., ethylene) is known to accelerate coking. Such olefins can be formed in the fuel mixing regions upstream of the reformer if residence times are too long and mixing is incomplete. Although not entirely quantitative, equilibrium predictions for stable graphite can provide a qualitative guide to where deposits may be problematic (Sasaki and Teraoka, 2003).

Figure 11 is a ternary diagram showing the region where equilibrium solid carbon is stable. These results are based on assuming that graphitic carbon is the only possible condensed phase. The deposit region depends upon composition and temperature. Hydrocarbons and most oxygenated fuels (e.g., alcohols) lie well into the deposit region. Syngas mixtures (i.e., mixtures of H_2 and CO) generally fall in the deposit-free region at typical SOFC operating temperatures. As steam and CO_2 are added to hydrocarbon fuels, the mixture tends toward the deposit-free region. The deposit-free region generally increases with increasing temperature.

5.6 Distributed charge transfer

The charge-transfer process is distributed over a region of a few tens of microns in the composite electrodes that surround the dense electrolyte membrane. Figure 12 shows profiles that are the result of solving the mass- and charge-conservation equations in a particular MEA structure (Zhu and Kee, 2008). The particular cell is operating at atmospheric pressure and 800°C on a fuel mixture of 97% H_2 and 3% H_2O air, with the oxidizer being air. The cell uses a 50-μm LSM–YSZ composite cathode, a 20-μm dense YSZ electrolyte, and a 550-μm composite Ni–YSZ anode. The nominal electrode particle diameters are 1 μm. Two solution profiles are shown, one at an operating voltage of E_{cell}=0.5 V and the other at E_{cell}=0.75 V. In both cases, the cathode interconnect is fixed at 0 V. More detail about the cell and operating conditions can be found in Zhu and Kee (Zhu and Kee, 2008), but the primary objective here is to explain and interpret the qualitative behaviors.

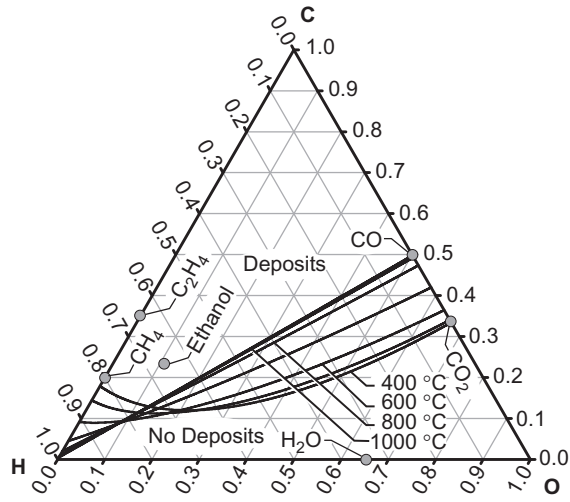

Figure 11 Ternary chart showing regions of equilibrium solid carbon (deposit) formation as functions of temperature and composition.

Electrons returning from an external circuit enter the cathode on the left-hand side. Because the electronic conductivities of the LSM and Ni are relatively high, very small gradients in the electron-conducting phases are not apparent on the scale of this plot. However, with YSZ having a relatively low ion conductivity, substantial electric-potential gradients are apparent in the ion-conducting phase. Because there is no charge transfer within the dense YSZ membrane, the electric-potential gradient of the ion-conducting phase is constant within membrane. Because the cell operating at E_{cell}=0.5V produces higher current, the electric-potential gradient is higher for the lower operating voltage. Because the membrane is assumed to be a pure ion conductor, the electric potential of the electron-conducting phase is not defined within the membrane. As discussed by Zhu and Kee (2008), the electrolyte electric potentials can be shifted by an arbitrary reference potential. The electrolyte electric potentials shown in Figure 12a are shifted such that they can be plotted in the same range of the electric potentials at the electronic-conducting phases.)

Figure 12b shows that purely electronic current (i.e., electrons) enters the cathode in the LSM phase and is gradually converted to ionic current in the YSZ phase over a thickness of about 5μm. The charge transfer proceeds at the TPB formed at the intersections of LSM and YSZ particles. The dense YSZ electrolyte admits only ionic current, which is uniform through the 20-μm electrolyte layer. On the anode side, ion current in the YSZ phase is gradually transferred to electron current in the Ni phase. For

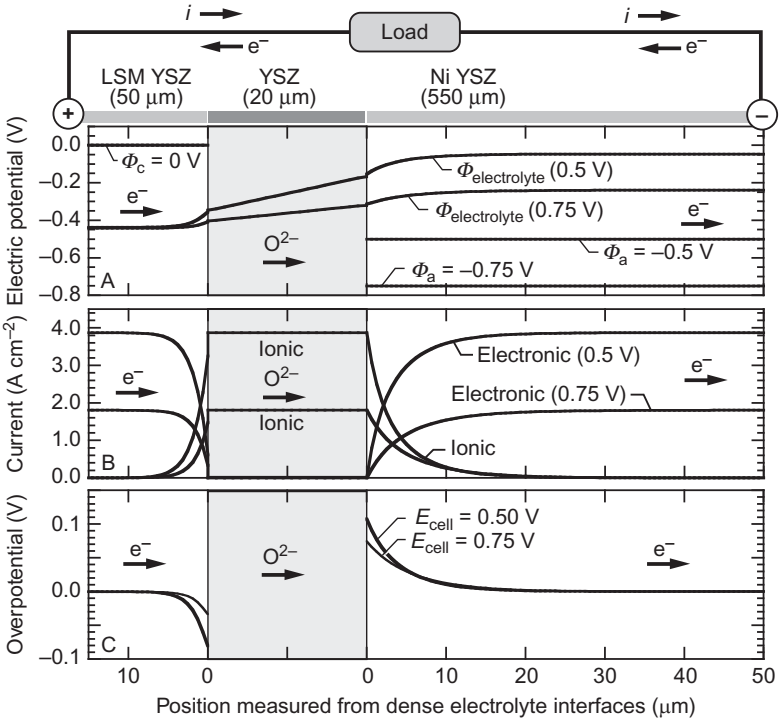

Figure 12 Profiles of electric potentials, current densities, and overpotentials through the electrochemically active region of a button-cell membrane-electrode assembly.

the parameters of this illustration, the charge transfer takes place over about 20μm on the anode side. At the lower cell potential of 0.5V, the current density is higher than at the higher cell potential of 0.75V. The sum of ionic and electronic current is the net current through the cell and the external circuit. The electron current leaves the cell and enters the external circuit. By definition, the direction of current i is opposite to the direction of electron transport.

Far from the dense electrolyte interfaces, Figure 12a shows that electrolyte-phase electric potentials are essentially flat and the current is purely electronic. The electric-potential profiles are flat because there is no charge transfer in these regions. Close to the dense electrolyte, charge-transfer rates are highest. Thus, the gradients in electric potentials and current density increase closer to the membrane interfaces. Because the effective ion conductivity within the porous electrodes is smaller than it is within the dense electrolyte, the slope of the electrolyte electric potentials within the electrodes but near the dense electrolyte is larger

than it is within the dense electrolyte. Charge-transfer rates are highest in the electrode regions nearest to the dense electrolyte interfaces.

Figure 12c shows the activation overpotential profiles (as would be used in the Butler–Volmer equations). Note that the overpotentials are negative on the cathode side, where the net charge-transfer process is cathodic (i.e., consuming electrons). The overpotentials are positive on the anode side, where the anodic charge transfer produces electrons.

5.7 Interface charge-transfer model

As illustrated in Figure 12, charge-transfer processes within the composite electrode are confined to a region of a few tens of microns around the dense electrolyte membrane. Therefore, the charge transfer for the thick electrode (order millimeter) can be reasonably approximated to occur within a vanishingly small distance from the dense electrolyte. The effective TPB length for the entire region is subsumed as an empirical parameter in the exchange current density. Additionally, because it is computationally expensive to resolve the distributed charge-transfer regions, the interface charge-transfer model is widely used. In this case, the modeling generally follows the approach that is discussed in Section 6.

6. CHANNEL-LEVEL MODELS

As a practical matter, models that represent chemistry and transport at the microscale of the MEA are too costly to incorporate into stack models at much larger length scales. At the channel scale, it is necessary to resolve fluid flow within channels or tubes (e.g., Figures 2 and 3). It is also important to predict the gas and solid temperature distributions along the lengths of channels. Full stacks can be represented as arrays of channels. Depending upon the intended application and available computation resources, each channel in the stack may be assumed to have identical behavior. In fact, however, depending upon the stack design (flow manifolds, thermal insulation, etc.), each channel performs differently.

6.1 Gas flow within channels

The gas-phase flow within planar channels or circular tubes is usually treated as a one-dimensional laminar plug flow, retaining only axial variations (Kee *et al.*, 2003; Zhu *et al.*, 2005). For syngas or methane fuels, homogeneous chemical kinetics are negligible for temperatures

below around 900°C (Gupta *et al.*, 2006b). The mass and momentum conservation equations are summarized as

$$\frac{\partial \rho}{\partial t} + \frac{\partial(\rho u)}{\partial x} = -\frac{P_\mathrm{h}}{A_\mathrm{c}} \sum_{k=1}^{K_\mathrm{g}} J_k^\mathrm{M} W_k \tag{51}$$

$$\frac{\partial(\rho u)}{\partial t} + \frac{\partial\left(\rho u^2\right)}{\partial x} = -\frac{\partial p}{\partial x} - \frac{P_\mathrm{h}}{A_\mathrm{c}} \tau_\mathrm{w}, \tag{52}$$

$$\frac{\partial(\rho Y_k)}{\partial t} + \frac{\partial(\rho Y_k u)}{\partial x} + \frac{\partial j_k}{\partial x} = -\frac{P_\mathrm{h}}{A_\mathrm{c}} J_k^\mathrm{M} W_k. \tag{53}$$

These equations are written in transient form, with the time t and the axial coordinate x being the independent variables. Dependent variables include the mass density ρ, the mean velocity u, the pressure p, and the species mass fractions Y_k. Geometric parameters include the hydrodynamic perimeter P_h and the cross-sectional flow area A_c. Assuming planar channel dimensions of H high and W wide, $P_\mathrm{h}=2(H+W)$ and $A_\mathrm{c}=HW$.

In addition to axial convective transport, there may be axial diffusion of species along the length of the tube. This is especially the case when gas velocities are low and species with high diffusion coefficients (e.g., H_2) are present. The axial diffusive mass fluxes are represented as

$$j_k = -\rho W_k \overline{W} D_{km} \frac{\partial X_k}{\partial x}. \tag{54}$$

The mixture-average diffusion coefficients are calculated as

$$D_{km} = \frac{1 - Y_k}{\sum_{\ell \neq k}^{K_\mathrm{g}} X_\ell / D_{k\ell}}, \tag{55}$$

where X_k are the mole fractions, and $D_{k\ell}$ is the multicomponent diffusion coefficient matrix, which can be evaluated from the binary diffusion coefficients $\mathcal{D}_{k\ell}$ (Kee *et al.*, 2003).

As a result of internal reforming and charge-transfer chemistry, species fluxes are exchanged between the porous-electrode structures and the flow within the channels. Molar fluxes of the gas-phase species, represented as J_k^M, are determined from the solution of the reactive porous-media transport within the electrode structures (Section 5.1).

Wall shear stress τ_w, which affects the pressure drop, is represented in terms of a friction factor $f=2\tau_\mathrm{w}/\rho u^2$. For a rectangular channel, the friction factor can be calculated based on the laminar, fully developed flows as $\mathrm{Re}\, f=C$. The local Reynolds number is defined in terms of the mean velocity u and the hydraulic diameter as $\mathrm{Re}=\rho u D_\mathrm{h}/\mu$, where μ is the mixture viscosity. The constant C depends upon the channel aspect ratio (Kee *et al.*, 2003).

Because the electrodes are relatively thin and the axial species gradients are small, axial species transport within the composite electrodes may be neglected. Transport and chemistry normal to the flow channel

can be represented in one-dimensional form using species and overall continuity equations (Equations (38) and (39)) as discussed in Section 5.1.

6.2 Channel-flow energy balance

Plug-flow energy balances are needed for both the fuel and air channels. The channel-flow models consider two temperatures—mean gas temperature within the channel (fuel mixture T_F and air T_A) and the solid MEA temperature T_M. The thermal balances include convective heat transfer between gas within the channels and the MEA structure as well as heat transport associated with species flux between the electrode and the adjoining gas.

Consider first the flow in the fuel channel, where gas-phase energy conservation can be expressed as

$$\frac{\partial E_F}{\partial t} + \frac{\partial q_F}{\partial x} = -\frac{P_h}{A_c}\left(q_a^T + q_a^M\right), \tag{56}$$

where $E_F = \rho_F e_F$, with ρ_F being the mass density and e_F being the specific internal energy of the fuel mixture. The gas-phase heat flux q_F, which represents both axial heat conduction and gas-phase species transport, is written as

$$q_F = -\lambda_F \frac{\partial T_F}{\partial x} + \sum_{k=1}^{K_g} \left(\rho Y_k u + j_k\right) h_k, \tag{57}$$

where h_k are the species specific enthalpies and λ_F is the mixture thermal conductivity.

The convective heat flux between the channel flow and the MEA structure is represented as

$$q_a^T = h_{conv}(T_F - T_M), \tag{58}$$

where h_{conv} is a convective heat-transfer coefficient, which may be evaluated using a conventional Nusselt-number correlation (Bergman *et al.*, 2011). As illustrated in Figure 13, the fluxes are defined as being positive when the flux leaves the gas channel and enters the MEA.

The second term on the right-hand side of Equation (56) (i.e., q_a^M) represents the energy transport associated with mass transfer between the channel flow and the porous anode structure (i.e., the MEA). Because all the heat release (i.e., resulting from thermal and electrochemical reactions and ohmic heat resistance) is assigned to the MEA structure, q_a^M must be subtracted from the conservative form of the channel-flow energy equation (Equation (56)). In the conservative form, the channel-flow energy equation implicitly contains the heat released within the porous electrode through the species continuity equations.

The heat flux associated with species transport between the MEA structure and the channel flow q_a^M can be written as

$$q_a^M = \sum_{J_k^M>0} J_k^M W_k h_k(T_F) + \sum_{J_k^M\le 0} J_k^M W_k h_k(T_M). \tag{59}$$

If species transfers from the channel into the MEA structure, enthalpies of the gas-phase species h_k are evaluated at the fuel-channel gas temperature T_F; otherwise, h_k are evaluated at the MEA temperature T_M. Note that $J_k^M>0$ indicates flux into the MEA.

With the directions of the fluxes being assigned as in Figure 13, the air-channel energy equation is entirely analogous to the fuel-channel equation. That is,

$$\frac{\partial E_A}{\partial t} + \frac{\partial q_A}{\partial x} = -\frac{P_h}{A_c}\left(q_c^T + q_c^M\right), \tag{60}$$

with the subscript ''c'' representing the air (cathode) channel.

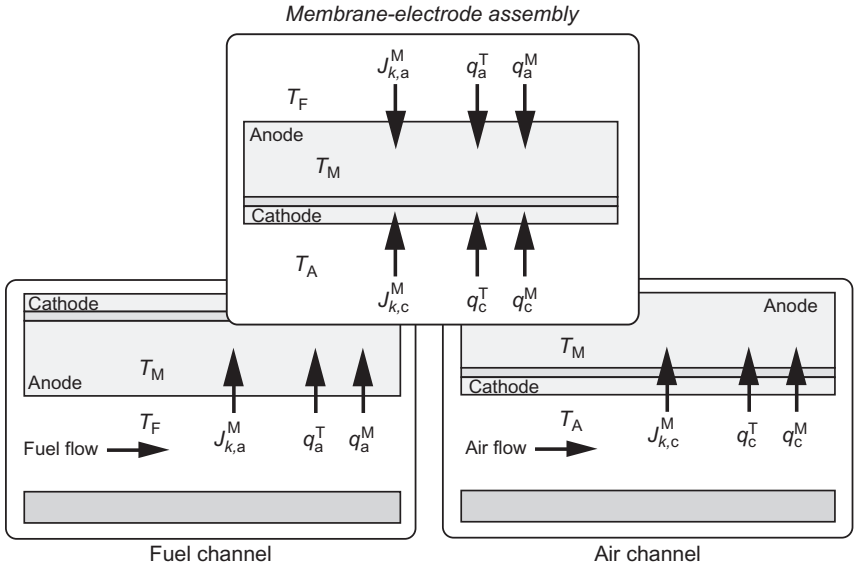

Figure 13 Illustration showing the directions of positive heat and mass fluxes between the flow channels and the MEA.

6.3 MEA energy balance

The MEA is assumed to have a uniform temperature normal to the flow direction, but varying axially. Further, the solid materials and the gas within the pore spaces are at a common temperature T_M. Energy conservation for the MEA structure may be written as

$$\frac{\partial E_M}{\partial t} + \frac{\partial q_M}{\partial x} = \dot{q}_M + \frac{P_F}{A_M} q_a^T + \frac{P_A}{A_M} q_c^T, \tag{61}$$

where E_M is the total internal energy per unit volume of the MEA structure, P_F is the width between fuel-side interconnect ribs, P_A is the width between air-side interconnect ribs, and $A_M = H_{anode} + H_{electrolyte} + H_{cathode}$ is the cross-sectional area (per unit depth) of the MEA, with H representing component thicknesses. The net volumetric heat source within the MEA structure, due to the thermal and electrochemical reactions and the ohmic resistance, may be written as

$$\dot{q}_M = \frac{P_F}{A_M} q_F^M + \frac{P_F}{A_M} q_A^M - \frac{P_M}{A_M} i_e E_{cell}. \tag{62}$$

In this equation, P_M is the perimeter of the dense electrolyte. Axial conduction within the MEA structure is written as

$$q_M = -\lambda_M \frac{\partial T_M}{\partial x}, \tag{63}$$

where λ_M is the effective thermal conductivity of the composite MEA structure.

6.4 Qualitative illustration

Figure 14 shows the qualitative behavior along the length of a fuel channel. Assuming that the interconnect structures are fabricated from a metal with high electrical conductivity, it is reasonable to assume that the cell voltage E_{cell} is spatially uniform. As fresh fuel enters the channel the reversible potential E_{rev} is high. However, as fuel is consumed and becomes diluted with reaction products (e.g., H_2O and CO_2), the reversible potential decreases. Because the current density depends upon the difference between the reversible potential and the cell voltage, the local current density also decreases. If the channel is sufficiently long, E_{rev} will approach the operating potential E_{cell}. At this point, the charge-transfer reactions can no longer proceed, causing the current density to vanish and eliminating any further fuel composition. Thus, there are operating conditions under which the fuel cannot be completely consumed. Indeed, it is the usual case that SOFC systems are operated with fuel utilization around 85%.

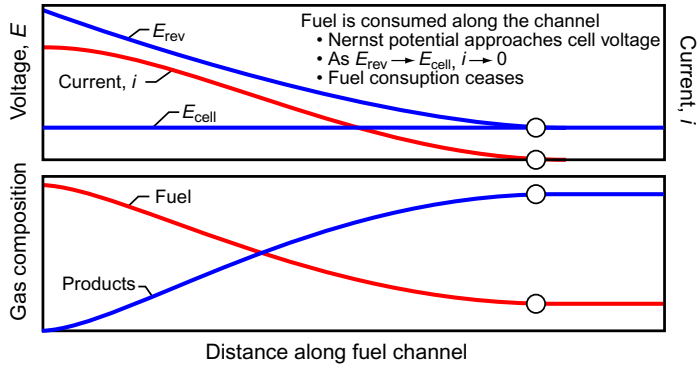

Figure 14 Qualitative behavior of fuel consumption, electrical current density, and reversible potential as functions of position along a fuel channel.

7. BUTTON CELLS AND PARAMETER FITTING

From the foregoing discussion, it is evident that numerous physical and chemical parameters are needed to model a practical cell. Although some parameters can be measured directly, many must be derived indirectly from experiments. Button-cell experiments are used widely in the development and evaluation of new materials and cell architectures. The most common experiments measure polarization characteristics (i.e., cell voltage as a function of current density). The experiments can readily be configured to measure performance at different temperatures and with different fuel compositions. Modeling data taken over a range of operating conditions can be used to determine needed parameters. Although the process can be time consuming, and without a guarantee of unique results, it is usually possible to develop reliable sets of parameters for particular cell architectures. Figure 15 shows measure and modeled polarization data for a particular cell that is being operated with either humidified H_2 or CH_4 (Pillai *et al.*, 2008). Button cells are highly valuable in the laboratory but have little value as practical fuel cells. However, the physical parameters that are established can be used to model other cell configurations that use the same or a similar MEA architecture (e.g., Figures 2–4).

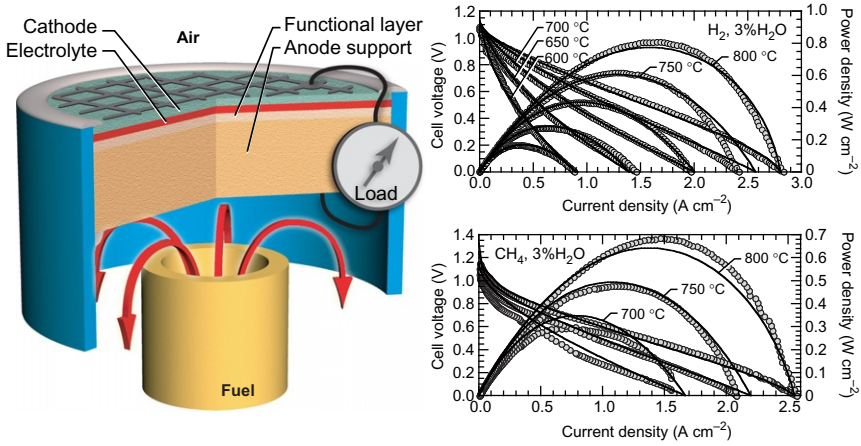

Figure 15 MEA models are usually developed to represent measured button-cell data.

8. ELECTROCHEMICAL IMPEDANCE SPECTROSCOPY

Fuel-cell performance is characterized by widely varying timescales. However, clearly isolating and identifying all the contributing physical and chemical processes can be difficult. Electrochemical impedance spectroscopy (EIS) provides a powerful means to probe behaviors that contribute to cell performance (Bard and Faulkner, 2000; Barsoukov and Macdonald, 2005; Bockris *et al.*, 2000).

Figure 16 illustrates the basis of EIS. A fuel cell, typically a button cell such as in Figure 15, is operated by drawing a low-amplitude harmonic current,

$$i_e(t) = \bar{i}_e + \hat{i}_e \sin(\omega t), \tag{64}$$

where ω is the frequency. As a result of the transient current, the corresponding cell voltage response is also harmonic but phase shifted:

$$E_{cell}(t) = \bar{E}_{cell} + \hat{E}_{cell} \sin(\omega t + \theta). \tag{65}$$

The phase shift θ and the ratio $\hat{E}_{cell}/\hat{i}_e$ depend upon the frequency and the nominal operating current $\bar{i}_e$. The complex impedance Z can be represented as

$$Z = \frac{\hat{E}_{cell}}{\hat{i}_e} e^{-j\theta} = \frac{\hat{E}_{cell}}{\hat{i}_e} (\cos\theta - j \sin\theta), \tag{66}$$

where $j \equiv \sqrt{-1}$. At a given frequency, the complex impedance can be represented as a point on a Nyquist plot as illustrated in Figure 16. Carrying out the procedure over a wide range of frequencies produces the impedance spectra.

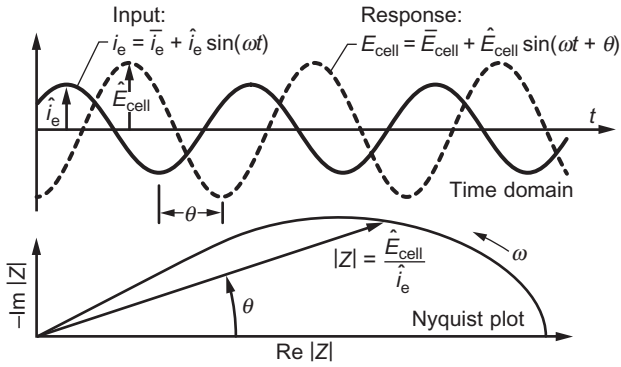

Figure 16 Qualitative aspects of electrochemical impedance spectroscopy.

Dedicated experimental equipment is readily available, and EIS is used widely in fuel-cell experiments. Experimental results are most commonly interpreted in the context of equivalent circuits using combinations of resistor and capacitor elements. Resistors are usually associated with ion transport processes and charge-transfer kinetics. Capacitors are usually associated with double-layer charging at the electrode–electrolyte interfaces as well as transient effects of gas transport and chemistry.

As an alternative to indirect equivalent-circuit representations, a very strong case can be made for interpreting impedance spectra directly with transient physical models. A time-accurate physical model is necessary, but there are alternative approaches to compute the EIS. One approach is to model exactly the experimental procedure, that is, impose a small-amplitude harmonic current, observe the voltage response, and compute the complex impedance (Zhu and Kee, 2006a). However, because the impedance must be computed at many different frequencies, this is a time-consuming process. State-space modeling, which transforms the mathematical problem to the frequency domain, has significant computational advantages (Bieberle and Gauckler, 2002; Mitterdorfer and Gauckler, 1999a,b,c). Bessler has reported a computationally efficient method in which the entire EIS can be recovered from a single transient simulation with a step or ramp variation of the current (Bessler, 2007).

Figure 17 illustrates EIS results for a button cell operating on humidified methane (Lin *et al.*, 2005; Zhu and Kee, 2006a). Electrochemical impedance is typically reported with the cell operating around open-circuit voltage (e.g., Figure 17a). As illustrated in Figure 17, the EIS is usually characterized by one or more ''arcs,'' with each arc representing some aspect of the underlying physics or chemistry. The two overlapping

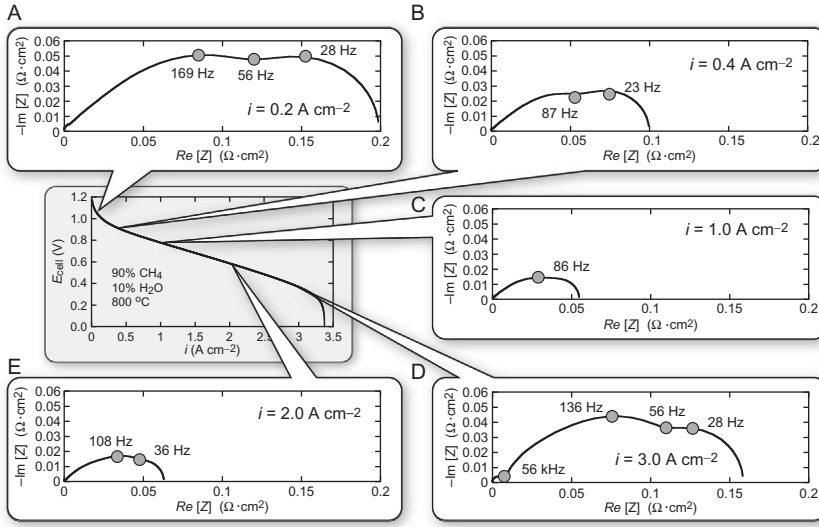

Figure 17 Computed electrochemical impedance spectra for an SOFC operating on humidified methane at 800 °C. The subplots shown in A-E are Nyquist representations of the complex impedance at different current densities.

low-frequency arcs are the result of interactions between porous-media transport and reforming chemistry. The results shown in Figure 17 do not include double-layer charging, which would typically contribute two more high-frequency arcs, one for the anode and the other for the cathode. The nearly linear shape of the EIS at high frequency is characteristic of diffusion impedance (so-called Warburg impedance). The net cell resistance is found by the difference in the intersections with the real axis. It is interesting to note that the shape of the EIS changes significantly for different cell polarization (i.e., different cell currents).

9. TUBULAR CELL PERFORMANCE

Figure 19 shows steady-state solution profiles for a particular SOFC tube, such as illustrated in Figure 18. The tube has an inner diameter of 0.8 cm and is 25 cm long. The porous Ni–YSZ anode tube wall is 900 μm thick, with an effective thermal conductivity of $10.5\,\mathrm{W\,m^{-1}K^{-1}}$. The electrolyte is 20 μm of YSZ and the cathode is 50 μm of porous LSM–YSZ. Other physical and chemical parameters are reported by Kee *et al*. (2008).

9.1 Steady-state performance

The inlet fuel is a mixture of 35.3% H_2, 14.2% CH_4, 1.3% CO, 41.3% H_2O, and 7.9% CO_2, which is the equilibrium output of a methane-steam reformer operating at 500°C and fed by a steam-carbon ratio of 2.5 (26.6% CH_4 and 71.4% H_2O). The fuel enters the tube with a mean velocity of $60\,\mathrm{cm\,s^{-1}}$, temperature of 750°C, and atmospheric pressure. The operating voltage is fixed at $E_{\mathrm{cell}}=0.75\,\mathrm{V}$, which is uniform for the entire tube length. There is convective heat transfer from the tube exterior, with the external air temperature being maintained at $T_a=750°\mathrm{C}$.

It is evident from Figure 19e that the gas and wall temperatures are significantly higher than 750°C, which is the temperature of the external air and the fuel inlet. Both the wall and fuel temperatures increase in the entry region of the tube, peaking at around 3 cm. The temperature increases are due to internal heat release within the MEA. In the entry region, the wall temperature is significantly higher than the temperature of the fuel gases. Because the tube wall has a relatively high thermal conductivity, heat can be transferred upstream toward the entrance. In the downstream sections, the flow temperature exceeds wall temperature. In this region, heat transfer to the relatively cool external air exceeds the MEA heat release, serving to reduce the MEA temperature. Internal heat generation, which scales approximately as i_e^2, decreases along the length of the tube as the current density i_e decreases. The fuel-flow temperature is also decreasing via heat transfer to the relatively cooler the wall.

Figure 19e shows that the gas velocity increases along the length of the tube. The steam reforming of methane produces a net mole increase (cf., Table 1), which serves to accelerate the flow.

Figures 19a–c show the gas-phase mole fractions in the pore spaces through the thickness of the porous anode (i.e., the tube wall). Based on the gradients of the concentration profiles, it is evident that H_2 diffuses into the anode (i.e., radially outward from the fuel flow toward the dense electrolyte), while the reaction products H_2O and CO_2 are transported radially inward from the MEA toward the fuel channel. Because only H_2 is consumed via charge-transfer chemistry in the three-phase region near the dense electrolyte interface (top of the upper panels). Methane diffuses radially outward where it is catalytically reformed by H_2O and CO_2 on the Ni surfaces, producing H_2 and CO. The CO and H_2O participate in the water-gas-shift process via catalytic chemistry on the on Ni surfaces within the anode structure. In the downstream sections, as the fuel is depleted and the current density decreases, the species gradients within the anode also decrease.

Figure 19d shows gas-phase mole-fraction profiles within the tube. As is easily anticipated, the fuel species (H_2, CO, CH_4) decrease, while

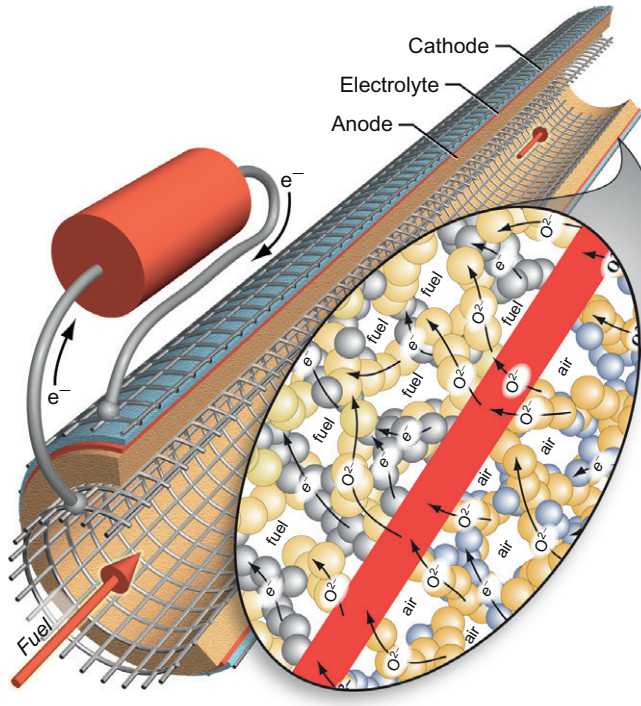

Figure 18 Illustration of an anode-supported SOFC tube. The balloon illustrates an idealized view of the MEA microstructure in the proximity of the dense electrolyte.

the product species (H_2O and CO_2) increase. For the parameters of this example, the flow at the tube exit still contains approximately 10% H_2, 2% CO, and 4% CH_4. In other words, the fuel utilization is low. In practice, such a circumstance would likely call for reduced inlet flow velocity, lower cell voltage, or increased temperature. Figure 19d also shows that the local current density decreases along the tube length, which is caused by the increasingly depleted and diluted fuel stream.

9.2 Efficiency and utilization

Cell performance is often measured in terms of conversion efficiency, fuel utilization, and power density (Zhu and Kee, 2006b). The cell efficiency is defined as

$$\varepsilon = \frac{W_e}{Q_{in}} = \frac{\int i_e E_{cell} dA}{\dot{m}_{f,in} \Delta h_{f,in}}, \tag{67}$$

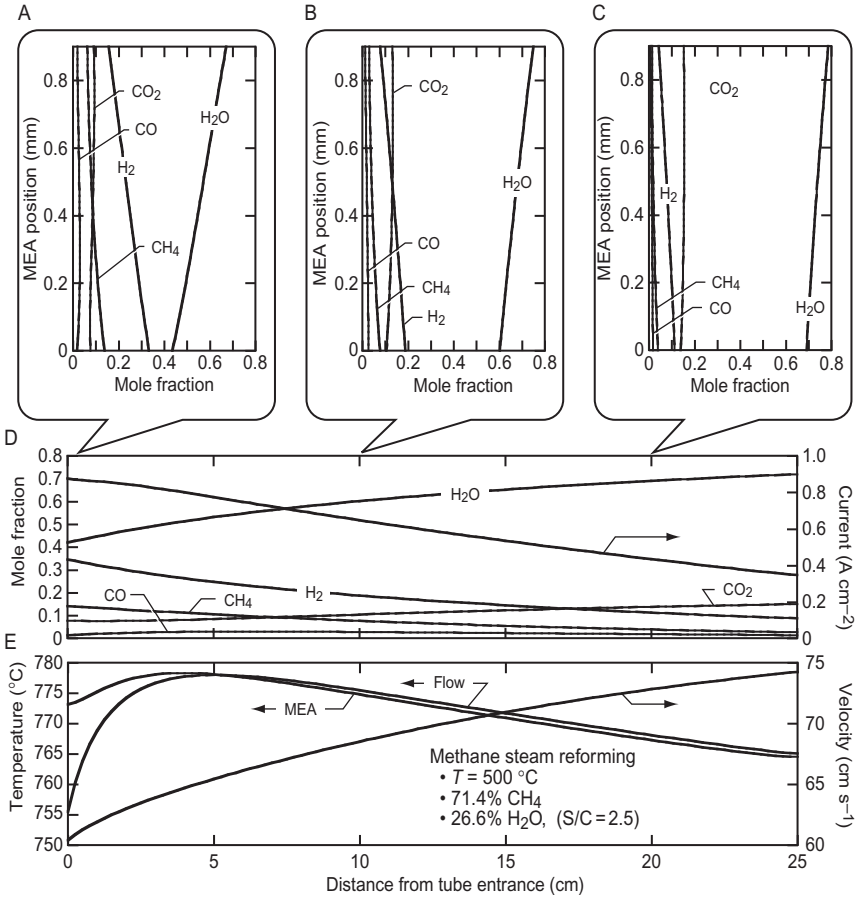

Figure 19 Solution profiles with an anode-supported tubular SOFC. The inlet fuel composition is the equilibrium output of a methane-steam reformer operating at 500°C with an input steam-carbon ratio of 2.5. The cell is operating with a uniform cell potential of E_{cell}=0.75V. The upper panels (A-C) represent gas-phase composition through the thickness of the anode support layer.

where W_e is the electrical work output and Q_{in} is the heat that would be released upon full oxidation of the inlet fuel stream. The inlet fuel mass flow rate is $\dot{M}_{f,in}$, and $\Delta h_{f,in}$ is the specific enthalpy associated with completely oxidizing the fuel stream. The electrical work is the product of the current density i_e and operating voltage E_{cell}, integrated over the active MEA area. Fuel utilization U can be written as

$$U = 1 - \frac{\dot{m}_{\mathrm{f,out}} \Delta h_{\mathrm{f,out}}}{\dot{m}_{\mathrm{f,in}} \Delta h_{\mathrm{f,in}}}, \tag{68}$$

where the ''in'' and ''out'' refer to the inlet and outlet of the fuel cell. The Δh refers to the specific enthalpy associated with complete oxidation of any available fuels. This definition accounts for the energy content of any remaining fuels (or fuel by-products) that leave in the fuel-cell exhaust. These definitions consider only performance within the SOFC, not overall system performance. The solution shown in Figure 19 results in efficiency of 48.2%, utilization of 71.4%, and a net power of 35.2 W.

9.3 Transient response

For control and load following, it is important to understand transient responses as a result of changes in operating conditions (Colclasure *et al.*, 2011). Figure 20 considers the same SOFC tube as in Figure 19 but in this case operating on a CPOX-generated fuel mixture consisting of 27.1% H_2, 25.2% CO, and 47% N_2. The cell is initially operating in steady state at a cell voltage of E_{cell}=0.9 V. At 100 s, the operating potential is suddenly reduced to E_{cell}=0.75 V. The reduced potential causes a nearly immediate increase in current from about 12 A up to about 20 A. At about 550 s, the voltage is suddenly increased to E_{cell}=0.85 V. This causes the current to decrease again to about 16 A.

Figure 20a shows that the current response to a change in cell voltage is nearly instantaneous. There is a slight overshoot in current, which relaxes as the fuel composition adjusts to the new operating condition.

Temperatures within the cell depend on internal losses and hence the operating conditions. With increased current, the cell temperatures begin to rise. Figure 20b shows the histories of the fuel-stream temperature and MEA tube-wall temperature at the tube exit. Because of thermal inertia in the solid materials, the temperatures respond much more slowly than the current. It takes nearly 300 s for the temperatures to reach new steady values at the higher current level. At around 550 s, when the voltage is again increased (thus, decreasing current), the temperatures begin to fall. Again the roughly 300-s time constants are evident. Cathode-air exhaust temperature is also shown. Because of relatively high air flow rates in this example, the cathode air maintains a considerably lower temperature than the tube.

Figure 20c shows species composition of the fuel stream at the tube exit. In this example, the fuel-flow rate is held fixed at m=4.8×10^{-6} kg s^{-1}, which corresponds to an inlet velocity of approximately 40 cm s^{-1}. In regions of high current, the concentrations of product species H_2O and CO_2 increase. Correspondingly, the fuel species H_2 and CO are more fully consumed. The time constant for species variations is determined primarily by the characteristic residence time for flow within the tube, which is

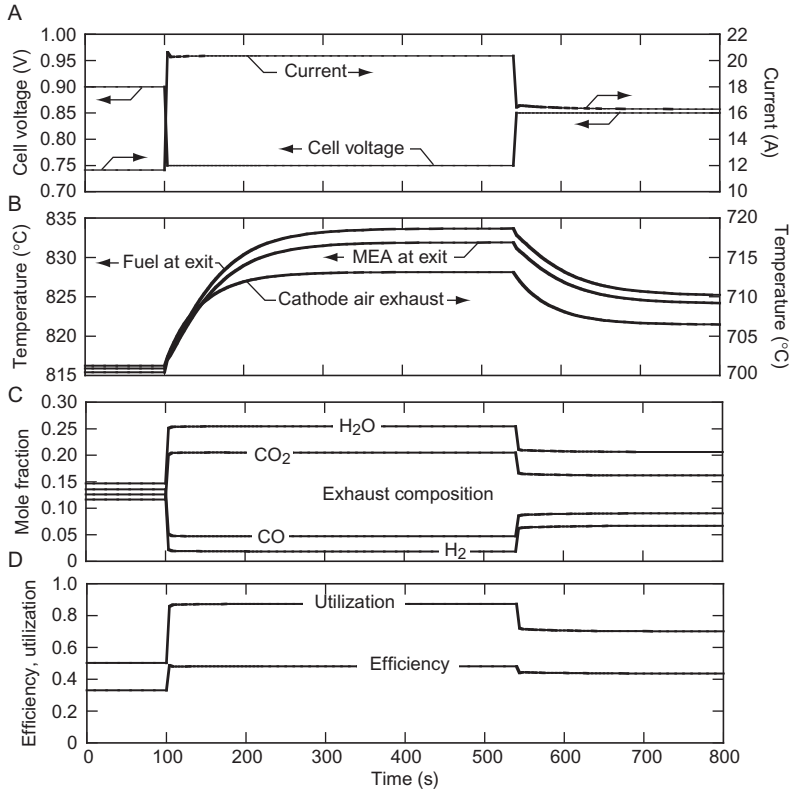

Figure 20 Transient responses of selected variables in an SOFC tube in response to a step change in cell voltage.

approximately 0.3s. Thus, with the timescale used in Figure 20, which is characteristic of the relatively long thermal timescales, the species changes appear immediate.

Figure 20d shows cell efficiency and fuel utilization. Initially, the efficiency is about 35% with a utilization of about 50%. When the cell voltage drops at about 100s, the efficiency increases to about 45% and the utilization approaches 90%. This illustration, which is intended to show transients in cell performance, uses a fixed fuel-flow rate. In practice, the fuel-flow rate could be controlled to compensate for variations in the cell potential and net power delivered.

10. COMPUTATIONAL IMPLEMENTATION

As is evident from the foregoing discussion, fuel cells may be modeled using significantly different levels of approximation. In all cases, the models manifest themselves as coupled systems of differential equations. Thus, appropriate initial and boundary conditions are needed, with details depending upon the particular model. Although certainly important, details of computational implementation are beyond the scope of this chapter. Nevertheless, models developed by the present authors follow some broad guidelines.

Spatial derivatives are usually discretized using the finite-volume method. Steady-state models, such as for button cells or fuel-cell channels, can be solved as boundary-value problems using a hybrid-Newton method (Grcar *et al.*, 1986; Kee *et al.*, 2003). Transient problems can be solved using a method-of-lines algorithm. However, it is usually the case that the differential equations involve algebraic constraints (i.e., equations without explicit time derivatives), leading to differential-algebraic equations (DAE) (Ascher and Petzold, 1998; Brenan *et al.*, 1996). High-level special purpose DAE software packages are available. These include LIMEX (Deuflhard *et al.*, 1987)[3] and DASSL,[4] which are written in FORTRAN, and SUNDIALS (Hindmarsh *et al.*, 2005; Serban *et al.*, 2005),[5] which is written in C++.

The governing equations involve thermodynamic properties and chemical reaction rates for multicomponent mixtures. When more than a few species and reactions are involved, the programming task is significantly facilitated by special purpose software that is designed to handle chemical complexity. Examples of such software include CHEMKIN (Kee *et al.*, 2003),[6] which is written in FORTRAN, and CANTERA (Goodwin, 2003),[7] which is written in C++.

There is a growing use of commercial Computational Fluid Dynamics (CFD) software to serve as a platform on which to build fuel-cell models. However, to date, there are no commercial packages that implement models with the level of chemical and electrochemical detail described in this chapter. Software such as ANSYS FLUENT can be extended with user-defined functions (UDF) to incorporate electrochemical complexity (Fluent software package; Goldin *et al.*, 2009; Kattke *et al.*, 2011). Software such as COMSOL[8] is a computational platform that solves systems of partial differential equations, allowing users to define details of the particular model.

[3] Download available from Konrad-Zuse-Zentrum für Informationstechnik Berlin: http://www.zib.de/ehrig/software.html.
[4] Download available from Prof. Linda Petzold, University of California, Santa Barbara: http://www.cs.ucsb.edu/~cse/index2.php?software.html.

11. SUMMARY AND CONCLUSIONS

Computational models of fuel cells can be developed to serve a wide range of purposes and objectives. Models that resolve microstructural electrochemistry and transport play valuable roles in the optimal design of electrode structures. Models that consider fluid flow and thermal transport at larger length scales play valuable roles in the optimal design of single cells and fuel-cell stacks. At the larger scales, however, it is computationally impractical to include the level of chemical and physical complexity that can be incorporated into a microstructural model. Although much can be learned from steady-state models, predicting transient response also plays important roles. Because of the thermal inertial associated with metal and ceramic components, SOFCs can have relatively long start-up and shutdown cycles. In load-following applications, process-control strategies that accommodate multiple sensors and actuators are needed to maintain high performance. Time-accurate transient models can be developed for incorporation into real-time process control.

Depending upon the objectives and computational resources, models must be written with significantly different levels of approximation. However, even when major approximations are required, it is important that the approximate models be as accurate as possible. Such time and length scale bridging enables the empiricism that is needed in the approximate models to be derived from the detailed models.

ACKNOWLEDGMENT

We gratefully acknowledge the support by the Office of Naval Research via an RTC grant (N00014-05-1-03339).

REFERENCES

Agnew, G. D., Collins, R. D., Jorger, M., Pyke, S. H. and Travis, R. P., *ECS Trans.* **7,** 105–111 (2007).

Ascher, U. M. and Petzold, L. R., Computer Methods for Ordinary Differential Equations and Differential-Algebraic Equations. SIAM, Philadelphia, PA (1998).

Bai, Y., Liu, J. and Wang, C., *Int. J. Hydrogen Energy* **34,** 7311–7315 (2009).

Bai, Y., Wang, C., Ding, J., Jin, C. and Liu, J., *J. Power Sour.* **195,** 3882–3886 (2010).

[5] Download available from Lawrence Livermore National Laboratory: https://computation.llnl.gov/casc/sundials/main.html.

[6] CHEMKIN is available commercially at: http://www.reactiondesign.com.

[7] Download is available at: http://code.google.com/p/cantera/.

[8] http://www.comsol.com/products/multiphysics/.

Bard, A. J. and Faulkner, L. R., Electrochemical Methods: Fundamentals and Applications. 2nd ed. Wiley, New York (2000).
Barsoukov, E. and Macdonald, J. R., Impedance Spectroscopy Theory, Experiment, and Applications. Wiley, Electrochemical Society, Penning-ton, New Jersey (2005).
Bergman, T. L., Lavine, A. S., Incropera, F. P. and Dewitt, D. P., Fundamentals of Heat and Mass Transfer. 7th ed. Wiley, Hoboken, New Jersey (2011).
Bessler, W. G., *J. Electrochem. Soc.* **154,** B1186–B1191 (2007).
Bessler, W. G., Gewies, S. and Vogler, M., *Electrochim. Acta* **53,** 1782–1800 (2007).
Bessler, W. G., Warnatz, J. and Goodwin, D. G., *Solid State Ionics* **177,** 3371–3383 (2007).
Bieberle, A. and Gauckler, L. J., *Solid State Ionics* **146,** 23–41 (2002).
Bockris, J. O., Reddy, A. K. N. and Gamboa-Aldeco, M., Modern Electrochemistry: Fundamentals of Electrodics. 2nd ed. Kluwer Academic/Plenum Publishers, New York (2000).
Brenan, K. E., Campbell, S. L. and Petzold, L. R., Numerical Solution of Initial-Value Problems in Differential Algebraic Equations. 2nd ed. SIAM, Philadelphia, PA (1996).
Chan, S. H., Chen, X. J. and Khor, K. A., *J. Electrochem. Soc.* **151,** A164–A172 (2004).
Chan, S. H. and Xia, Z. T., *J. Electrochem. Soc.* **148,** A388–A394 (2001).
Chen, D., Lin, Z., Zhu, H. and Kee, R. J., *J. Power Sour.* **191,** 240–252 (2009).
Colclasure, A. M., Sanandaji, B. M., Vincent, T. L. and Kee, R. J., *J. Power Sour.* **196,** 196–207 (2011).
Costamagna, P., Costa, P. and Antonucci, V., *Electrochim. Acta* **43,** 375–394 (1998).
DeCaluwe, S. C., Zhu, H., Kee, R. J. and Jackson, G. S., *J. Electrochem. Soc.* **155,** B538–B546 (2008).
Deuflhard, P., Hairer, E. and Zugck, J., *Num. Math.* **51,** 501–516 (1987).
Feduska, W. and Isenberg, A. O., *J. Power Sour.* **10,** 89–102 (1983).
Fluent software package, version 13.0, ANSYS Inc. see also www.ansys.com.
Gardner, F. J., Day, M. J., Brandon, N. P., Pashley, M. N. and Cassidy, M., *J. Power Sour.* **196,** 122–129 (2011).
Goldin, G., Zhu, H., Kee, R. J., Bierschenk, D. and Barnett, S. A., *J. Power Sour.* **187,** 123–135 (2009).
Goodwin, D. G., *In* ''Chemical Vapor Deposition XVI and EUROCVD 14'' (M. Allendorf, F. Maury and F. Teyssandier, Eds.), PV 2003-08, pp. 155–162. Electrochemical Society (2003) see alsohttp://www.cantera.org (2003).
Goodwin, D. G., *In* ''Solid Oxide Fuel Cells IX'' (S. Singhal and J. Mizusaki, Eds.), pp. 699–707. Electrochemical Society, Wiley, Hoboken, New Jersey (2005).
Goodwin, D. G., Zhu, H., Colclasure, A. M. and Kee, R. J., *J. Electrochem. Soc.* **156,** B1004–B1021 (2009).
Gostovic, D., Smith, J. R., Kundinger, D. P., Jones, K. S. and Wachsman, E. D., *Electrochem. Solid-State Lett.* **10,** B214–B217 (2007).
Grcar, J. F., Kee, R. J., Smooke, M. D. and Miller, J. A., *Proc. Combust. Inst.* **21,** 1773–1782 (1986).
Grew, K., Peracchio, A. A., Izzo, J. R. and Chiu, W., *ECS Trans.* **25,** 1861–1870 (2009).
Gubner, A., Nguyen-Xuan, T., Bram, M., Remmel, J. and de Harrt, L., Lightweight cassette type SOFC stacks for automotive applications. European Fuel Cell Forum, Luzern, Switzerland, Paper B042, 2006 (2006).
Gunda, N. S. K., Choi, H.-W., Berson, A., Kenney, B., Karan, K., Pharoah, J. G. and Mitra, S. K., *J. Power Sour.* **196,** 35923603 (2011).
Gupta, G. K., Dean, A. M., Ahn, K. and Gorte, R. J., *J. Power Sour.* **158,** 497–503 (2006).
Gupta, G. K., Hecht, E. S., Zhu, H., Dean, A. M. and Kee, R. J., *J. Power Sour.* **156,** 434–447 (2006).
Hecht, E. S., Gupta, G. K., Zhu, H., Dean, A. M., Kee, R. J., Maier, L. and Deutschmann, O., *Appl. Catal. A* **295,** 40–51 (2005).

Hindmarsh, A. C., Brown, P. N., Grant, K. E., Lee, S. L., Serban, R., Shumaker, D. E. and Woodward, C. S., *ACM Trans. Math. Softw. (TOMS)* **31**(3), 396 (2005).
Howe, K. S., Thompson, G. J. and Kendall, K., *J. Power Sour.* **196,** 1677–1686 (2011).
Isenberg, A. O., *Solid State Ionics* **3–4,** 431–437 (1981).
Iwai, H., Shikazono, N., Matsui, T., Teshima, H., Kishimoto, M., Kishida, R., Hayashi, D., Matsuzaki, K., Kanno, D., Saito, M., Muroyama, H., Eguchi, K., Kasagi, N. and Yoshida, H., *J. Power Sour.* **195,** 955–961 (2010).
Izzo, J. R., Jr., Joshi, A. S., Grew, K. N., Chiu, W. K. S., Tkachuk, A., Wang, S. H. and Yun, W., *J. Electrochem. Soc.* **155,** B504–B508 (2008).
Janardhanan, V. M. and Deutschmann, O., *J. Power Sour.* **162,** 1192–1202 (2006).
Kattke, K. J., Braun, R. J., Colclasure, A. M. and Goldin, G., *J. Power Sour.* **196,** 3790–3802 (2011).
Kee, R. J., Coltrin, M. E. and Glarborg, P., Chemically Reacting Flow: Theory and Practice. John Wiley, Hoboken, NJ (2003).
Kee, R. J., Zhu, H. and Goodwin, D. G., *Proc. Combust. Inst.* **30,** 2379–2404 (2005).
Kee, R. J., Zhu, H., Sukeshini, A. M. and Jackson, G. S., *Combust. Sci. Technol.* **180,** 1207–1244 (2008).
Lin, Y., Zhan, Z., Liu, J. and Barnett, S. A., *Solid State Ionics* **176,** 1827–1835 (2005).
Mason, E. A. and Malinauskas, A. P., Gas Transport in Porous Media: The Dusty-Gas Model. American Elsevier, New York (1983).
McIntosh, S., He, H., Lee, S., Costa-Nunes, O., Krishnan, V. V., Vohs, J. M. and Gorte, R. J., *J. Electrochem. Soc.* **151,** A604–A608 (2004).
Metcalfe, C., Kesler, O., Rivard, T., Gitzhofer, F. and Abatzoglou, N., *ECS Trans.* **25,** 1185–1194 (2009).
Minh, N. Q., *J. Am. Ceram. Soc.* **76,** 563–588 (1993).
Mitterdorfer, A. and Gauckler, L. J., *Solid State Ionics* **117,** 187–202 (1999a).
Mitterdorfer, A. and Gauckler, L. J., *Solid State Ionics* **117,** 203–217 (1999b).
Mitterdorfer, A. and Gauckler, L. J., *Solid State Ionics* **120,** 211–225 (1999c).
Moyer, C. J., Sullivan, N. P., Zhu, H. and Kee, R. J., *J. Electrochem. Soc.* **158,** B117–B131 (2011).
Nam, J. H. and Jeon, D. H., *Electrochim. Acta* **51,** 3446–3460 (2006).
Pillai, M. R., Gostovic, D., Kim, I. and Barnett, S. A., *J. Power Sour.* **163,** 960–965 (2007).
Pillai, M. R., Jiang, Y., Mansourian, N., Kim, I., Bierschenk, D. M., Zhu, H., Kee, R. J. and Barnett, S. A., *Electrochem. Solid-State Lett.* **11,** B174 (2008).
Rüger, B., Joos, J., Weber, A., Carraro, T. and Ivers-Tiffée, E., *ECS Trans.* **25,** 1211–1220 (2009).
Sanyal, J., Goldin, G. M., Zhu, H. and Kee, R. J., *J. Power Sour.* **195,** 6671–6679 (2010).
Sasaki, K. and Maier, J., *Solid State Ionics* **134,** 303–321 (2000).
Sasaki, K. and Teraoka, Y., *J. Electrochem. Soc.* **150,** A878–A888 (2003).
Serban, R., Shumaker, D. E., Hindmarsh, A. C., Lee, S. L., Brown, P. N., Grant, K. E. and Woodward, C. S., *ACM Trans. Math. Softw.* **31,** 363–396 (2005).
Shearing, P. R., Golbert, J., Chater, R. J. and Brandon, N. P., *Chem. Eng. Sci.* **64,** 3928–3933 (2009).
Smith, J. R., Chen, A., Gostovic, D., Hickey, D., Kundinger, D., Duncan, K. L., DeHoff, R. T., Jones, K. S. and Wachsman, E. D., *Solid State Ionics* **180,** 90–98 (2009).
Tomida, K., Kabata, T., Hisatome, N., Yamashita, A., Tsukuda, H., Ohkuma, S. and Kiyabu, T., *ECS Trans.* **7,** 173–180 (2007).
Vogler, M., Bieberle-Hütter, A., Gauckler, L., Warnatz, J. and Bessler, W. G., *J. Electrochem. Soc.* **156,** B663–B672 (2009).
Vural, Y., Ma, L., Ingham, D. B. and Pourkashanian, M., *J. Power Sour.* **195,** 4893–4904 (2010).
Wilson, J. R., Cronin, J. S., Duong, A. T., Rukes, S., Chen, H., Thornton, K., Mumm, D. R. and Barnett, S. A., *J. Power Sour.* **195,** 1829–1840 (2010).

Wilson, J. R., Duong, A. T., Gameiro, M., Chen, H., Thornton, K., Mumm, D. R. and Barnett, S. A., *Electrochem. Commun.* **11,** 1052–1056 (2009).
Wilson, J. R., Gameiro, M., Mischaikow, K., Kalies, W., Voorhees, P. W. and Barnett, S. A., *Microsc. Microanal.* **15,** 71–77 (2009).
Wilson, J. R., Kobsiriphat, W., Mendoza, R., Chen, H. Y., Hiller, J. M., Miller, D. J., Thornton, K., Voorhees, P. W., Adler, S. B. and Barnett, S. A., *Nat. Mater.* **5,** 541–544 (2006).
Yurkiv, V., Starukhin, D., Volpp, H.-R. and Bessler, W. G., *J. Electrochem. Soc.* **158,** B5–B10 (2011).
Zhan, Z. and Barnett, S. A., *Solid State Ionics* **176,** 871–879 (2005).
Zhu, H. and Kee, R. J., *J. Power Sour.* **117,** 61–74 (2003).
Zhu, H. and Kee, R. J., *J. Electrochem. Soc.* **153,** A1765–A1772 (2006a).
Zhu, H. and Kee, R. J., *J. Power Sour.* **161,** 957–964 (2006b).
Zhu, H. and Kee, R. J., *J. Electrochem. Soc.* **155,** B175–B729 (2008).
Zhu, H. and Kee, R. J., *J. Power Sour.* **18,** 7654–7664 (2011).
Zhu, H., Kee, R. J., Janardhanan, V. M., Deutschmann, O. and Goodwin, D. G., *J. Electrochem. Soc.* **152,** A2427–A2440 (2005).